We are very grateful to the three referees for their detailed and fruitful comments which have allowed us to clarify various points. We copy-pasted below their reviews. Comments from Reviewers #1, #2 and #3 are in red, green and blue, respectively. For each comment/suggestion, our responses are in bold black and the revised/additional text in italic black. We also provide a track-change manuscript at the end of the present document.

Also, please note that we gathered all the questions/comments about the curve fitting (pseudo-observations) in the same paragraph (pages 5-6)

General and specific comments

Reviewer #1

Information about data and code availability is lacking. Under "Data availability" the authors give http://community-inversion.eu as the reference for the code, however, this is just a general website about the CIF. This website indicates the Git git.nilu.no/VERIFY/CIF but this is just for the generic version of CIF and not that pertaining to this paper. Also, under this section, details about where to access the observational and prior flux data should be given.

We included a DOI for this version of the CIF and additional information about where to access the observational and prior flux data.

The code files of the CIF version used in the present paper are registered under the following link : https://doi.org/10.5281/zenodo.6304912. Prior anthropogenic fluxes (EDGARv4.3.2) can be downloaded from the EDGAR website (https://edgar.jrc.ec.europa.eu/dataset_ghg432). Biomass burning fluxes can be downloaded from the GFED website (https://globalfiredata.org/pages/data/). Prior natural fluxes and other data are available upon request (joel.thanwerdas@lsce.ipsl.fr). Many stations from different networks contributed to the CH4 data used in the present paper (a comprehensive list can be found in the supplement and in the acknowledgments). Their data is freely available upon request to the station maintainers or via dedicated websites. The $\delta^{13}C(CH_4)$ observational data can be downloaded from the NOAA-GML website (https://gml.noaa.gov/dv/data/).

P1L2: suggest changing this to: "…indicating relative changes in the sources and sinks" as it is evident from the fact that the mixing ratios have been increasing that there must be a change in the sources and/or sinks and not just a variation but a change in one relative to the other.

We agree and, following your suggestion, this part of the sentence has been modified.

P2L13: I think this sentence is potentially confusing and could be better formulated. What I think the authors mean is that without regularization the inverse problem is ill-conditioned (or ill-posed) giving no unique solution, hence the need for regularization e.g. by providing prior information. Also it is unclear to me what is meant by "no continuity with the data" - could the authors please explain this.

We apologize for not making this sentence clear enough. An ill-posed problem is often defined as a problem which may have more than one solution but also in which the solutions depend discontinuously upon the initial data. In an inversion problem, the data referred to the atmospheric observations and we know that a small change in this data could result in a radically different solution. We used your suggestion to modify this sentence and make it more intelligible.

Without regularization of the problem, e.g. providing prior information, the inverse problem is ill-conditioned (or ill-posed). It means that there is no unique solution to the problem but also that a small error in the assimilated data (here atmospheric observations) can result in large errors in the derived solution.

P2L21: Variational methods, such as the Lanczos version of the conjugate gradient algorithm provides the posterior error covariance matrix with little additional computational cost.

We agree with the reviewer. We should have added that we consider our inversion problem (our observation operator) as non-linear because we include isotopic observations in our data. The Lanczos version of the conjugate gradient algorithm can be utilized only if the observation operator is linear. We also included a little discussion on this in Sect. 3.5 and in the conclusions because using the Lanczos method to provide posterior uncertainties is an important perspective of our work. However, it necessitates further developments and to clarify whether our observation operator and therefore our cost function can be linearized without affecting our results.

Thus, the variational formulation is preferred to the others when optimizing emissions and sinks at the pixel scale using large volumes of observational data, although its main limitation is the numerical cost to access posterior uncertainties when there is non-linearity in the inversion problem (Berchet et al, 2021).

P2L33-34: I would suggest the authors give ranges for the various source categories to reflect how variable values within each category can be.

We agree with this suggestion. Although we preferred not to mention the minimum and the maximum provided by Sherwood et al. (2017) because using isotopic data would appear less relevant to the reader. We preferred to include the mean and standard deviations for each source process.

CH_4 isotopic source signatures $\delta^{13}C(CH_4)_{source}$ notably differ between emission categories ranging from ^{13}C-depleted biogenic sources (−61.7 ± 6.2 ‰, one standard deviation) and thermogenic sources (−44.8 ± 10.7 ‰) to ^{13}C-enriched thermogenic sources (−26.2 ± 4.8 ‰) (Sherwood et al., 2017; Schwietzke et al., 2016), although the distribu-tions are very large and overlaps exist between the extreme values.

P3L2: I think the authors should precise that they are not consistent with the d13C observations and the prescribed d13C ratios.

We added a sentence to elaborate.

Saunois et al. (2017) pointed out that many emission scenarios inferred from atmospheric inversions are not consistent with $\delta^{13}C(CH_4)$ observations and that this constraint must be integrated into the inversion systems to avoid such inconsistencies. In addition, they highlighted the sensitivity of the atmospheric isotopic signal to the source partitioning and prescribed isotopic ratios.

P3L12: Thompson et al. 2018 used a variational method to optimize CH4 emissions and the OH sink with the AGAGE 12-box model. Perhaps the authors mean never in a variational inversion framework with a full 3D atmospheric transport model?

Yes, we apologize because we were not clear enough and writing that, we unintentionally diminished the work of Thompson et al. (2018). We modified this sentence following your suggestion.

The implementation of such a constraint in an inversion system have already been attempted in previous studies focusing on CH_4 (e.g., Thompson et al., 2018; McNorton et al., 2018; Rigby et al., 2017; Rice et al., 2016; Schaeferet al., 2016; Schwietzke et al., 2016; Rigby et al., 2012; Neef et al., 2010; Bousquet et al., *2006; Fletcher et al., 2004) but, to our knowledge, never in a variational system associated to a 3-D chemistry-transport model (CTM).*

P4L15: All Bayesian methods require the inverses of R and B.

We agree and modified this sentence.

As in analytical and ensemble methods, the variational formulation necessitates the inversion of both error matrices R and B.

P4L17: I think you should specify the assumption, i.e. that the observation errors are uncorrelated.

We agree and modified this sentence.

R is considered diagonal as point observations are distant in time and space (i.e., uncorrelated observation errors), allowing for the inverse to be calculated easily, although that assumption should be revised with the increasing availability of satellite sources.

EQ6-7: I'm confused about the value MTOT, is this the molar mass of CH4 in source FiTOT, if so then MTOT depends on the d13C ratio of CH4 in FiTOT.

We apologize for not mentioning this in the submitted manuscript. In our study, we set M_{TOT} (M_T in the revised manuscript), the total CH_4 molar mass, to a constant value of 16.0415. As of now, this value can be freely defined by the user before starting the inversion but remain constant throughout the minimization. Molar masses are involved only to convert CH_4 mass fluxes into $^{12}CH_4$ and $^{13}CH_4$ mass fluxes in the forward and tangent-linear runs and also to perform the equivalent operation in the adjoint run. We demonstrate very quickly here that the $\delta^{13}C(CH_4)_{source}$ range of values observed in the CH_4 sources would result in a negligible variation around the chosen value and would very likely not affect the results of our study or that of any other inversion performed with our system.

To make the demonstration, we take the $^{12}CH_4$ and $^{13}CH_4$ molar masses provided by Stolper et al. (2014) :
M_{12} = 16.031 g/mol
M_{13} = 17.035 g/mol

By definition of the total CH4 molar mass, here denoted MT, we have :

$$M_T = \frac{M_{12} + A \cdot M_{13}}{1 + A}$$

with

$$A = (1 + \delta^{13}\mathrm{C}(\mathrm{CH4})) \cdot R_{\text{std}}$$

In this case, $\delta^{13}C(CH_4)_{source}$ can roughly vary between -70 ‰ and -10 ‰. It gives M_T = 16.041384 and M_T = 16.042046, respectively, thus a variation of 0.004 %. In Eq. 5 and 6 in the manuscript, both right-hand members are divided by M_T, hence the same value is applied to both fluxes. As ratios between $^{12}CH_4$ and $^{13}CH_4$ quantities are more important than the $^{12}CH_4$ and $^{13}CH_4$ values, we expect the impact of setting the total CH_4 molar mass constant to be highly negligible.

Deriving tangent-linear and adjoint operations while including the relationship above would result in an overly complex code and would very likely not influence the results.

We added some explanations to the manuscript.

M_T should preferably depend on M_{12} and M_{13} when converting the mass fluxes:

$$M_T = \frac{M_{12} + A^i \cdot M_{13}}{1 + A^i}$$

However, the complexity of the forward, tangent-linear and adjoint codes would be largely enhanced by such a relationship. The code structure would also be less generic, i.e., it could not be used for other isotopologues of CH_4, such as $\delta D(CH_4)$. We choose to implement M_T as a constant that can be prescribed freely by the user, therefore without considering any influence of the prescribed M_{12} and M_{13} values, also prescribed by the user. As the observed isotopic source signatures roughly vary between −70 ‰ and −10 ‰, a maximum variation of 0.004 % in M_T could be expected. It will very likely not affect the results of our study or that of any other inversion performed with our system.

P7L13: For the category "fossil fuels" could the authors please specify if this is only fugitive emissions or also combustion emissions, and if the source signature is considered the same for fugitive and combustive emissions?

As mentioned in the main manuscript, we adopted the prior CH4 emissions compiled for inversions performed as part of the Global Methane Budget (Saunois et al., 2020). The Table below shows the relationship between our subcategories and those of EDGARv4.3.2.

The EDGARv4.3.2 categories PRO_OIL and PRO_GAS (fugitive emissions during oil and gas exploitation) largely contribute (~90 %) to the total of the "Oil, Gas & Industry" subcategory. Therefore, we chose to ignore the influence of other subcategories on the isotopic signature of the category. We added this sentence to the text :

The EDGARv4.3.2 categories PRO_OIL and PRO_GAS (fugitive emissions during oil and gas exploitation) largely contribute (~90 %) to the total of the "Oil, Gas & Industry" sub-category. Therefore, we chose to neglect the influence of other subsub-categories (such as industry) on the isotopic signature of the category.

Combining sectors

Grouped sector	EDGAR categories	Description	Propagation	IPCC categories
Coal	HDC	hard coal	Combined. Then scaled by BP.	1B1a
	BRC	brown coal		
Oil, Gas & industry	OIL	Oil exploration, production, transportation, refining and storage	Scaled by BP.	1B2a1 + 1B2a2 + 1B2a3 + 1B2a4
	GAS	Natural gas venting and flaring	Scaled by BP.	1B2c
	PRO – (OIL + GAS)	Oil evaporation from trucks and tankers + gas from pipelines.	This is not scaled. It is kept constant.	?
	TNR (All)	Transport ex road – All Aviation, Shipping, Railways etc.	Linearly propagated to 2017.	1A3a_CDS + 1A3a_CRS + 1A3aLTO + 1A3a_SPS + 1A3c + 1A3e + 1A3d + 1C2
	TRO	Road transport	Linearly propagated to 2017.	1A3b
	CHE	Chemical processes	Combined. Then linearly propagated to 2017.	2B
	IRO	Iron and steel production		2C1c + 2C1d + 2C1e + 2C1f + 2C2
	ENE	Power industry	Combined. Then linearly propagated to 2017.	1A1a
	IND	Combustion for manufacturing		1A2
	REF_TRF	Oil refineries and transformation industry		1A1b+1A1c+1A5b1+1B1b+1B2a5+1B2a6+1B2b5+2C1b

P9L2: I think it would be good to include the references for the source signatures in the main part of the manuscript and not just in the supplement. Also, there is no reference given for the livestock category nor an explanation why this category had a time varying source signature and what the dependence on time was.

The references for the source signatures have been included in the main part of the manuscript (Table 1). The livestock reference was in the main part of the manuscript (P7L28). We added some explanation about the time varying component and reworded the sentences.

Livestock isotopic source signatures are taken from Chang et al. (2019) and aggregated into the 11-regions map by selecting region-specific values. Livestock source signatures have been likely decreasing over time since the 1990s due to changes in C3/C4 diet within the major livestock producing countries and therefore annual values are prescribed. However, these estimates end in 2013 and we set the years 2014 to 2017 equal to the year 2013. Consequently, only the year 2012 has a different prescribed value from the other years.

P10L7: Do the authors mean that the model, LMDZ-SACS cannot reproduce the high temporal frequency of CH4 or d13C or both? If it is d13C, weekly observations are not high frequency. Also do the authors have an idea why the temporal variability could not be reproduced? I think this needs to be better explained. Also why assimilating the curve fitted data was chosen as the solution rather than e.g. increasing the observation uncertainty, filtering or averaging the observations?

Curve fitting data:
- Was there any specific reason why you decided to use smoothed data?
- After curve fitting, what is the temporal resolution of the data you assimilated? Did you generate same amount of δ 13 C(CH4) data in REF and S2?

Using Smoothed Observations

I note the comment on Page 10. “The observed high- frequency temporal variability cannot be adequately reproduced by the LMDz-SACS model. Therefore, instead of assimilating the real observations, we used a smooth curve fitting the real observations.” This is both striking and concerning. We noted from the earliest days of using high-frequency observations in formal inversions (Law et al., 2002, 2003; Peylin et al., 2005) that much of the power of high-frequency measurements came from the interplay between variations in meteorology and concentration. Abandoning this deserves more comment. What evidence do you have of the failure of LMDZ-SACS to simulate such observations? If you are using smoothed concentrations do you smooth the meteorology or the simulated concentration and (potentially) sensitivity the same way?

We apologize for not making this part of the explanation clearer. LMDz is obviously capable of reproducing high-frequency temporal variability. However, in this study, we focused on constraining monthly and annual flux variations (i.e. long-term trend and seasonal cycle) rather than investigating daily or weekly variations. Therefore, when assimilating isotopic observations, we quickly noticed that the monthly and annual components of the isotopic time-series had much more impact on the results than weekly (potentially large) variations in the observations.

Using the curve fitted data is equivalent to taking all observations, but with correlations in the R matrix. But as we do not want to invert a R matrix that is non-diagonal, we prefer to use pseudo-observations, filtering out the high-frequency signal.

Also, before running the inversions, we thought that maybe, using the curve fitted data would reduce the computational burden of the inversion and facilitate the convergence. However, considering S2 results, we were wrong. We chose to curve fitted the data because it appeared to be the best way to preserve the long-term trend as well as the seasonal cycle in the most intelligent way, following

Masarie and Tans (1995). We sampled the pseudo-observations at the same time as the real observations.

When referring to observations that have a "high temporal frequency", we meant observations that are not monthly or yearly averages. The term was misleading and we changed that.

In this study, we focused on estimating monthly and annual flux variations rather than investigating daily or weekly variations. Prescribing error correlations in the R matrix (introduced in Sect. 2.1) can be used to ensure that the inversion preferentially constrains the components we are interested in (i.e., long-term trend and seasonal cycle). In order to keep the R matrix diagonal and to focus on monthly and annual variations of the signal, we chose to use $\delta^{13}C(CH_4)$ observational data based on a curve fitting the original $\delta^{13}C(CH_4)$ observations. The fitting curve is a function including 3 polynomial parameters (quadratic) and 8 harmonic parameters as in Masarie and Tans (1995). After the fitting, the pseudo-observations were sampled at the same time as the original observations. We also hypothesized that the convergence would be slightly faster if a smooth curve fitting the real observations was used instead of the real observations, which appeared to be false (see Sect. 3.1). One sensitivity inversion aims at estimating the error introduced by this simplification (simulation S2 in Table 2).

Fig. 3a) I think here "cost" (or "value of cost function") is meant and not "cost function" and it would help to specify that the x-axis is "iterations".

Following your suggestion, we modified this.

Section 3.1: I think somewhere the results of the adjoint tests should be presented since a new version of the model was developed, including its adjoint.

In the main text :
In order to confirm that the several adjoint operations have been correctly implemented, we also provide the results of multiple adjoint tests in the supplement (Text S4).

In the supplement (Text S4) :

The adjoint code test is based on the definition of the adjoint observation operator :

$$\langle \boldsymbol{H}\delta\boldsymbol{U}, \boldsymbol{H}\delta\boldsymbol{U}\rangle = \langle \delta\boldsymbol{U}, \boldsymbol{H}^*\boldsymbol{H}\delta\boldsymbol{U}\rangle$$

In practice, the vector $\delta U=\lambda\cdot U$ is first provided as an input to the tangent-linear model, with λ being a scalar. After this, the output vector δU is retrieved and the first scalar product (left-hand member) is calculated. The adjoint code is then run with this vector as input. The output vector $H^*H\delta U$ of this adjoint code is recovered and the second scalar product is computed. The ratio of these two scalar products is then compared to the machine error (or machine epsilon), here denoted by ε, which gives the upper limit of the approximation error caused by the rounding of the calculations of the machine used. The adjoint test value, here denoted by r, is therefore defined by :

$$r = \frac{\frac{\langle \boldsymbol{H}\delta\boldsymbol{U}, \boldsymbol{H}\delta\boldsymbol{U}\rangle}{\langle \delta\boldsymbol{U}, \boldsymbol{H}^*\boldsymbol{H}\delta\boldsymbol{U}\rangle} - 1}{\epsilon}$$

With the LMDz-SACS model, a valid adjoint code should not result in a r exceeding 1000 and this ratio is usually between 1 and 300 for a valid code. Adjoint tests were performed with a machine error of $2.220446049250313 \times 10^{-16}$ (double-precision). We run two tests involving a two-month simulation based on the REF configuration. Both tests apply an increment λ of 0.2. The first test applied the increment in the control space (x) whereas the second does it in the minimization space ($\chi = B^{-1/2} \cdot (x - x^b)$) as explained in Berchet et al. (2021).

The other configurations only modify the input data (fluxes, source signatures, prescribed errors) and do not influence the adjoint operations performed during the inversion, hence we present only the results with REF.

The first test gave a ratio of 50 whereas the second test provided a ratio of 5, proving that the adjoint operations were properly implemented.

P14L16-19: Could the decreasing values of d13C in REF be also due to an underestimation of the atmospheric sink since reactions with OH and Cl enrich d13C?

Yes, we completely agree and it has been added in the text.

P18L20: It would be helpful if it would be stated again that this is for NOISO and REF increments.

It has been added.

P19L6: It is interesting that in order to correct for the prior decreasing trend in d13C, the inversion increases the source signatures of all sources, this means that the increases in the d13C rich sources, such as biofuel/biomass burning, are not sufficient to correct this trend. In T3 and T4 these emissions increased significantly, since there was not the degrees of freedom to adjust the source signatures. The question is, what is more accurate, higher source signatures or high d13C rich sources? Also, this result depends of course on having the correct atmospheric sink. Although these questions cannot be answered in this paper, I think they warrant more discussion as these are key sources of uncertainty. Also, I think the statement “All source signatures are shifted upwards by the inversions” needs to be qualified, that is, there are the exceptions of T3 and T4 (which had very small prior uncertainties for the sources signatures) and the “natural” source.

This is a very interesting suggestion. We included some discussion about it at the end of Sect. 2.5.4. We also clarified the statement “All source signatures are shifted upwards by the inversions”.

These results must be interpreted with caution because the input data suffer from high uncertainties. The artificial increase of the source signatures by our system can be hardly related to literature and former investigations. Consequently, it is challenging to conclude whether an increase of the source signatures would be more realistic (i.e., supported by observational data) than, for instance, only increasing the emissions of 13C-enriched sources such as BB. This system is only based on a mathematical and physical framework connecting the several groups of uncertainties (observational, prior fluxes, prior source signatures, prior sinks) and finding the most likely solution. Better estimates of these uncertainties must be prescribed before obtaining robust results. In particular, the uncertainties on KIE values and sink intensities have not been tested here and could largely influence the results. Also, the prescribed uncertainties on source signatures are relatively smooth in REF compared to recent estimates (Sherwood et al., 2017). Assessing these uncertainties should be a key aspect for future studies using this new inversion system to quantify the global CH_4 budget.

P19L9: I think by “total fractionation effect” the authors mean the kinetic isotope effect of atmospheric oxidation, if so, I suggest changing this to be clearer about what is meant. Also, I think it would be interesting to include a test using alternative OH fields to see how strongly the results are affected by the OH sink estimate.

This has been modified. At first, we thought about including tests using alternative OH fields (with/without inter-annual variability, with different spatial distributions, with different intensities) but we decided to limit ourselves to pure technical tests and not scientific ones in order to show only the technical potential of the system. Another study, still in preparation, is focusing on OH uncertainties with this new assimilation system. It should be submitted before the end of the year.

P19L14:18: Presumably this describes the results of the REF scenario, but it would be clearer to specify this.

We clarified this.

The WET global source signature, associated with REF posterior estimates, exhibits the larger upward shift compared to prior estimates…

Reviewer #2

1. non-Negative Constraints

Is there a non-negative constraint on either emissions or isotopic signatures? I doubt this since it is (or was) not easy to do in the M1QN3 algorithm used here. It is, though possible by routines in the scipy minimisation suite that still offer the same limited memory capability. The advantages can be large since a non-negative constraint removes the risk of large positive-negative flux dipoles which can inflate the posterior uncertainty.

There is no non-negative constraint on either emissions or isotopic signatures. We noticed that a highly negligible part of the posterior fluxes were negative (< 0.02 Tg/yr globally) due to the prescribed uncertainty of 100 %. This problem appears to be much less important for isotopic signatures as both positive and negative signatures can theoretically be observed, albeit positive signatures are very unlikely. The prescribed uncertainties on these signatures are, in any case, too small to lead to positive signatures in posterior estimates. We think this problem is beyond the scope of this study and discussing it in the main text could only result in an overly complicated story for the reader. It will nevertheless be addressed in future CIF developments and we are grateful to the reviewer for mentioning the scipy minimisation suite.

Spin-up and Spin-down

You noted on Page 18 "However, flux and source signature estimations of the 2012-2013 and 2016-2017 periods are not interpreted as the system appears to require a 2-year spin-up (2012-2013) and a 2-year spin-down (2016-2017), over which the inversion problem is not sufficiently constrained and isotopic signatures vary widely over time.". This is intriguing. It occurs, if I understand correctly, despite a long spin-up with 2012 fluxes to roughly equilibrate isotopic ratios at the start of the inversion period. Do you do this for every iteration as the control vector is up- dated? (I doubt this, it would be very expensive.) I am particularly surprised by the spin-down problem. We are used to the idea that CO 2 fluxes, at least, are only really constrained by observations a few weeks into the future. After that atmospheric mixing homogenises the Jacobian too much. Hence fluxes too close to the end of a run might lack constraint. There might be a reason why isotopic ratios would have much longer-lasting sensitivities but this isn't obvious to me and deserves some explanation.

Here, we are referring to the inversion spin-up, namely the fact that there is a potential lag between the constraint brought by the observations and the associated feedback on the fluxes / isotopic signatures. For CH4-only inversions, this spin-up and spin-down times are generally shorter than a year, if not six months. At first, we were surprised to notice such an effect but, given the very long relaxation timescales of isotopic ratios in the atmosphere (Tans et al., 1997), it seems coherent. Fully understanding this would require a lot of time and running multiple inversions (or possibly only tangent-linear simulations), starting from different initial conditions spanning the prescribed uncertainty envelope, to infer until when the initial atmospheric isotopic ratios and/or isotopic source signatures can influence the time-series of atmospheric isotopic ratios. This was too much work for this study but will certainly be addressed in future studies.

These long effects are certainly caused by the relatively long relaxation timescales of isotopic ratios in the atmosphere (Tans et al., 1997) compared to that of total CH_4. Fully understanding this would require a lot of time and running multiple inversions (or possibly only tangent-linear simulations), starting from different initial conditions spanning the prescribed uncertainty envelope, to infer until when the initial atmospheric isotopic ratios and/or isotopic source signatures can influence the time-series of atmospheric isotopic ratios. This is however beyond the scope of this study.

Computational Cost

The authors dwell on this a good deal. It seems almost a metric of a given set-up is its convergence rate. I suggest de-emphasising this. While I sure calculation time was frustrating it is mainly caused by the parallellisation limits on LMDZ-SACS. If these restrictions were reduced, as they already are in some other models, this would be a less important point. It is also certain to reduce in importance as models improve.

It is a very interesting point. We agree it is mainly due to the parallelization limits of LMDz-SACS. We tried to be as comprehensive as possible on this because we think the user/reader can benefit from our experience and easily reduce the computational burden of an inversion. The S1 and T1 setups do not largely affect the results and can easily be adapted to reduce the number of iterations. We also indicated the number of hours of simulation per CPU because the inversions we performed here are relatively short compared to what would be required to rigorously investigate atmospheric methane mysteries, such as the 2000-2006 stabilization, the subsequent renewed growth or the recent large increase rates. Even with more CPUs, we suppose (hope) that the computational burden will always be a problem (decision criterion), especially if we also consider the carbon footprint of such simulation / inversion. In addition, there is a trend toward increasing the spatial resolution of CTMs in order to, for instance, assimilate a huge amount of high-resolution satellite data. It leads to a rebound effect : the more we manage to reduce computational burden, the more we want to increase spatial resolution. Finally, we also emphasized this point because we do have solutions that we mentioned in the conclusion and that could lead to an even more powerful system. For all these reasons, we think it is worth emphasizing the computational burden of the inversions performed with our system.

Reviewer #3

Presentation of novelty

As authors mention very briefly, this is a first attempt to carry out variational inversion assimilating δ13C(CH4) observations. Please mention this also in the abstract, and add slightly more details of the development in the Introduction, e.g. development of adjoint and implementation in CIF. From the Introduction, I was also not sure if such modelling has been done with LMDz previously, i.e. how well LMDz have been simulating δ13C(CH4)?

As mentioned by Reviewer #1, this is the first attempt to carry out variational inversion assimilating $\delta^{13}C(CH_4)$ but only with a 3-D chemistry-transport model. Nevertheless, we agree with the reviewer that this has to be emphasized in the abstract and in the introduction. This is not the first official attempt to simulate $\delta^{13}C(CH_4)$. Another one of our papers, describing the impact of the Cl sink on CH_4 and $\delta^{13}C(CH_4)$, was previously submitted to the ACP journal (Thanwerdas et al., 2019) but was rejected, albeit not because of modeling error. We added some information in the text.

Abstract :

To our knowledge, this represents the first attempt to carry out variational inversion assimilating $\delta^{13}C(CH_4)$ with a 3-D chemistry-transport model (CTM) and to independently optimize isotopic source signatures of multiple emission categories.

Introduction :

This new system was implemented in the Community Inversion Framework (CIF), supported by the European Union H2020 project VERIFY (http://www.community-inversion.eu) and required to implement new forward, tangent-linear and adjoint operations. The forward operations were previously used to estimate the impact of the Cl sink on the modeling of CH_4 and $\delta^{13}C(CH_4)$ in LMDz (Thanwerdas et al., 2019).

Categorization of the simulations

I was not completely convinced about those S and T groups. Are they really needed? Did you categorize them based on results or really expected T groups to have higher variation before you started simulations? T1 is not only about changing isotope signature values and their uncertainty, but also the degree of freedom (dof) in the optimization (I guess you optimize 10 flux categories?).

We chose to use S and T groups to facilitate the presentation of results. At the beginning of the writing, no groups were used and the reading was very fastidious. We therefore decided, based on multiple feedbacks from different readers, to create the S-group using the simulations that were expected to give little variation. Based on preliminary results, it was quite easy to predict which simulations were going to be in the S-group before even running our full simulations. The remaining simulations were included in another group. We think that the reader can more easily follow the presentation of the results knowing whether a simulation has largely affected or not the results just by seeing the name of the simulation.

At the beginning, we predicted that the T1 simulation was going to be in the S-group. However, final results provided evidence that we could not reasonably include this simulation in the S-group as the variation was somehow too large for the S-group but too small for the T-group. We thought about creating a third group but it would have resulted in a presentation of results and a discussion likely difficult to read. Including the T1 simulation in the T-group but showing all the values from the T-group in Figure 6 and Figure 7 was the best compromise we found.

We recognize that this splitting may seem cumbersome at first. However, we tested many very different reading configurations and it was almost impossible to concisely and clearly present and discuss the results without these groups. We deeply apologize but we did not find any rewording, correction or addition that may resolve your concern.

Discussion on results

Although this technical paper is not meant to evaluate the flux estimate nor δ13C(CH4) values obtained from the simulations, I would like to see briefly how your estimates are compared to previous studies. Or even simply mentioning in the Conclusion how you would do further analysis, including e.g. availability of evaluation data.

We provide some additional thoughts about further analyses in the conclusion. However, we do not think this study is appropriate for comparisons with other estimates as the period 2012-2017 is never used as a period of interest in the litterature. Therefore, we prefer not to include any comparisons that could be misinterpreted. Longer periods are often selected to study the 2000-2006 stabilization and the subsequent regrowth periods. A paper, focusing on the 1998-2018 period and using the same system, is already in preparation and should be submitted by the end of the year. Some information about this new study is therefore provided in the conclusion.

As mentioned in the introduction, future work will address the estimation of CH_4 emissions over longer periods of time using this new system. For instance, the 2000-2006 CH_4 stabilization period and the subsequent renewed growth are particularly interesting to study using the isotopic constraint as global $\delta^{13}C(CH_4)$ started to decrease after 2006. These periods of time have already attracted considerable critical attention from many inversion studies (with or without the isotopic constraint) and comparing the results derived from such a complete 3-D variational inversion system with other recent estimates should be highly relevant. The most important limitation of assimilating $\delta^{13}C(CH_4)$ lies in the fact that very limited $\delta^{13}C(CH_4)$ data are available, and therefore evaluating the posterior simulated $\delta^{13}C(CH_4)$ is often challenging, if not impossible. However, satellite and balloon / AirCore data can easily be used to evaluate the posterior simulated CH_4.

Discussion on uncertainty estimates

I understand that it is costly to calculate the full uncertainty from all simulations. However, you anyway present uncertainty in P12 L12. How was it calculated? From the cost function, you can speculate how dof and inclusion of additional data would affect the posterior uncertainty. Please comment on it in Section 3.5.

We suppose the reviewer is referring to page 21. We did not include much details on this part and we apologize for that. Following your recommendations, we therefore included some additional information and discussion. We calculated the full uncertainty range using the minimum and maximum values among all the configurations, as in Saunois et al. (2020). At present, this method is the only one we can use, although it is insufficient. In particular, this method does not address the fact that some configurations are less likely and less realistic than others.
The inclusion of additional $\delta^{13}C(CH_4)$ will likely not affect the posterior uncertainty significantly because we expect the uncertainties on isotopic source signatures to have a much larger influence. We are not sure what the reviewer means by "how dof would affect the posterior uncertainty ?". The posterior uncertainties of the fluxes associated to the subcategories will likely be equal or slightly larger than that of the fluxes associated to the categories but it is very difficult to speculate on this.

Formally, posterior uncertainties are given by the Hessian of the cost function. This matrix can hardly be computed at an achievable cost considering the size of the inverse problem. Other means must be implemented to get posterior uncertainty such as estimating lower-rank approximation of the Hessian, using Monte-Carlo ensembles of variational inversion to represent the prior uncertainties or computing multiple configurations covering a given range of possibilities. Here, using multiple configurations provides insight into the posterior uncertainty associated with the posterior fluxes. We calculated the full uncertainty range using the *minimum and maximum values among all the configurations, as in Saunois et al. (2020). WET, AGW, FF and BB flux estimates (Table 3) exhibit an uncertainty of 10 %, 7 %, 19 % and 38 %, respectively. BB is the most uncertain estimate relative to its intensity, although FF shows the largest absolute uncertainty (23 $TgCH_4.yr-1$). These uncertainties are unlikely to be affected by the assimilation of additional $\delta^{13}C(CH_4)$ data because we expect the uncertainties on the isotopic source signatures to have a much larger influence. However, this remains to be tested in future work if posterior uncertainties can be calculated.*

At present, M1QN3 is not the only optimization algorithm that can be utilized to perform variational inversions in the CIF. The CONGRAD algorithm (Fisher, 1998), that follows a conjugate gradient method combined with a Lanczos algorithm, is also implemented. In particular, it considerably facilitates the computation of posterior uncertainties. Any change in algorithm is very easy and accessible to any CTM embedded in the CIF. However, CONGRAD has not been tested yet with δ13C(CH4) data. As CONGRAD is only designed for linear problems, using this algorithm could radically change the results of inversions performed with the isotopic constraints and future work will focus on using CONGRAD to perform the inversions with isotopic constraints.

Distribution of state vectors: did you assume all to be normal/Gaussian?

We are not sure what the reviewer means by "distribution of state vectors". The errors associated with the control vector (can also be called state vector) and the observation vector are assumed, indeed, to be normal/Gaussian. This is already mentioned in Sect. 2.1.

How did you derive the aggregated signature values?

Prescribed isotopic signatures are chosen based on literature values (Text S1 in the submitted manuscript, Table 1 in the revised manuscript). Apart from wetlands, regional values (or one global value if not enough data available) are chosen and assigned on a map at LMDz spatial resolution. The $^{12}CH_4$ and $^{13}CH_4$ fluxes for all subcategories are then derived based on Eq. 6 and 7 and added up. The resulting fluxes are then converted back to a $\delta^{13}C(CH_4)_{source}$ map representing the aggregated isotopic signature of the category. We included the part of this explanation that was missing in the manuscript (Sect. 2.4.1).

To infer the $\delta^{13}C(CH_4)_{source}$ *map of a category based on the sub-categories, the* $^{12}CH_4$ and $^{13}CH_4$ *fluxes for each emission sub-category within a category are derived based on Eq.5 and 6 and added up. The resulting fluxes are then converted back to a* $\delta^{13}C(CH_4)_{source}$ *map representing the aggregated isotopic signature of the category.*

What is the temporal and spatial resolution of prior fluxes?

Prior fluxes are prescribed at monthly resolution (following the EDGARv4.3.2 resolution) and at the spatial resolution of the LMDz model (3.8° x 1.9°). We added a sentence in Sect. 2.4.1 :

All prior fluxes are prescribed at monthly resolution and at the spatial resolution of LMDz.

What is the temporal resolution of the optimization?

Three values per month (10 days, 10 days and the rest) for the fluxes and their associated isotopic signatures are included in the control variables. This was mentioned in Sect. 2.4.1.

Can you provide range of observation uncertainty (diagonals of R) for each stations, maybe by adding information in Table S3 and S4, and briefly mention ranges in the main text? This will help understanding the results on cost function and RMSE differences better.

We find this suggestion highly relevant and we added this information for each station in Table S3 and Table S4. We also added a brief sentence in the main text, in Sect. 2.4.2.

These errors range between 3-19 ppb for CH_4 observations and 0.11-0.20 ‰ for $\delta^{13}C(CH_4)$ *observations. Mean prescribed errors for each station are provided in the supplement (Tables S3 and S4).*

Offsets in initial condition: How much offset did you need to add/subtract?

We applied an offset of +1.4 ‰ to $\delta^{13}C(CH_4)$ initial conditions. It has been added to the text.

P13 L9: "Consequently, the system is preferentially adjusting δ13C(CH4) over CH4 values to reduce the cost function."

• Can you speculate why? Is it because observation uncertainty (diagonals of R) is relatively smaller in δ 13 C(CH4) than CH4 ? The cost function show that the observational constraint in CH 4 is larger (probably main reason is amount of data?).

We added some explanation / speculation to the text.

Consequently, the system is preferentially adjusting $\delta^{13}C(CH_4)$ over CH_4 values to reduce the cost function, presumably because the ratio of RMSE to prescribed observational error for $\delta^{13}C(CH_4)$ is, on average, about twice as large as for CH_4. In other terms, it is simpler for the system to adjust $\delta^{13}C(CH_4)$ before attempting to modify CH_4. The ratio of the number of $\delta^{13}C(CH_4)$ observations to the number of CH_4 observations is not expected to play a significant role in the convergence process, although we did not rigorously study this influence. This ratio is only expected to affect the contribution of a component ($\delta^{13}C(CH_4)$ or CH_4) to the total cost function.

• For S2, I wonder why contributions of δ13C(CH4) and CH4 are similar to S3. Did you assimilate same amount of δ13C(CH4) data in REF and S2?

Yes, after the curve fitting, we sampled the pseudo-observations at the same time as the real observations. Therefore, we have the same amount of data in REF and S2. We added some explanation about the sampling following your other comment above about the curve fitting.

P14 L30-34: This could also be due to prescribed observation/transport model uncertainty.

It is likely not due to this because mean observation errors prescribed for these stations are large (10-15 ppb) but not the largest among all the assimilated stations (up to 18-19 ppb). We added this sentence to the main text.

Prescribed observation errors are likely not the main cause because mean values for these stations are large (10-15 ppb) but not the largest among all the assimilated stations. It can also be due to transport error or misrepresentation of sources close to the sites.

Emission increments: Emission changes are large in regions with high emissions. Please mention.

We agree with this comment and added this to the main text.

Overall, increments are large in regions with high emissions.

Please expand how much work would be needed for switching transport models and optimization methods in CIF for the δ13C(CH4) data assimilation. Can we use e.g. initial mixing ratios, do we need to run spin-up and build adjoint if transport model is changed? How about changes in optimization methods? Can we use same state vectors and covariance structures?

We included some additional information about switching transport models and optimization methods.

The major drawback of this inversion system is undoubtedly the large computational burden of a full minimization process. At least 40 iterations appear to be necessary to reach a satisfying convergence state at the regional scale. For the LMDz-SACS model, a maximum of 8 CPUs can be run in parallel, resulting in an elapsed time of 5-6 weeks to run one of the inversions of this study. A new generation of transport models such as DYNAMICO (Dubos et al., 2015) could help to address this problem in the future by allowing more processors to run in parallel. Also, further developments will implement some parallelization methods to enable computational burden reduction (e.g., Chevallier, 2013). In addition, variational inversions as implemented in the CIF are not enabled to provide a quantification (even approximated) of the posterior uncertainties. Dedicated efforts need to be done to address this issue in the future, at an achievable numerical cost. In particular, using the CONGRAD algorithm instead of M1QN3 could be a solution as both algorithms can be easily selected in the CIF. However, additional work is needed to ensure that switching the minimization algorithm does not affect the results inferred with our new system.

This system is implemented within the CIF framework and can therefore be used for inversions with the various CTMs embedded in the CIF, provided the adjoint codes of the models exist. As the operations developed for the purpose of this study are performed outside the model structure, forward, tangent-linear and adjoint codes and adjoint codes from other CTMs do not require any modifications as long as the model is capable of simulating both $^{12}CH_4$ and $^{13}CH_4$ simultaneously. The prior input must be adapted to the new model (spatial and time resolution) but the format of the observational data and of the prescribed errors can be preserved. Also, due to the variational method benefits, the efforts dedicated to the preparation of inputs do not scale with either the size of the observational datasets or the length of the simulation time-window. Therefore, this system is very powerful and is particularly relevant to study in a consistent way the influence of multiple physical parameters on atmospheric isotopic ratios, such as the transport, the isotopic signatures, the emission scenarios, the KIE values, etc. We did not try to assess here the sensitivity of the system to these parameters as only technical aspects of the system were tested. This will be part of future analyses.

Figure 3: Please add label of x-axis

This has been done.

Figure 4: Please add legend of posterior results from REF simulation, and perhaps use different color than green, as it's not S-group simulation? Please also add results from NOISO.

We added the legend associated with the REF simulation and applied a different color. For the $\delta^{13}C(CH_4)$ panel, posterior NOISO global source signature is -54.1 ‰ and the NOISO line would reach lower values than PRIOR REF in 2017, resulting in an image even more zoomed out and therefore affecting the clarity. We therefore do not suggest to include NOISO but we mention it in the caption. For CH_4, the line is actually extremely close to the REF line and it would also affect the clarity to include it. We also include this explanation in the caption.

The NOISO lines were not included because 1) the posterior NOISO global source signature is -54.1 ‰ and the line would therefore reach lower values than the REF PRIOR, affecting the visual clarity of the upper plot. 2) The NOISO CH_4 values are extremely close to the REF values and including it would also affect the clarity of the lower plot.

Figure 4 caption: I guess the figure is global monthly mean?

Yes. We modified the caption.

Figure 5: Prior CH_4 is same for all simulations, and $\delta^{13}C(CH_4)$ for some. Please consider minimizing.

We strongly recommend not to minimize the plot. A lower number of boxes in only one or two panels would force us to adapt the x-labels and the box colors depending on the panel. We think that it would strongly affect the visual clarity of the plot. We nevertheless reduced the number of station labels in the lower-left panel as they are all the same.

Figure S2: Please add label and unit of y-axis. Caption is slightly unclear – what do you mean by "inferred with REF"?

We added the label and modified the caption to make it clearer.

Technical comments

P3L2: constrain -> constraint
This has been modified.

P3L3: have -> has
This has been modified.

P3L6: regrowth -> renewed growth
This has been modified.

P4L16: This phrase is not grammatically correct, please change to "allowing for the inverse to be calculated easily"
This has been modified.

P5L18: multi-constrain -> multi-constraint
This has been modified.

P12L3-L16: This would be easier to follow if the list items (i.e. the different inversion tests) would be numbered.
This has been modified.

P19L6: source signature -> source signatures
This has been modified.

P21L16: relatively -> relative
This has been modified.

P14 L22: The S-group provides a better match to δ13C(CH4) observations than…
This has been modified.

P15 L4-5: AMY is not in South-East Asia.
We changed this to "South-East and East Asia".

Variational inverse ~~modelling~~ modeling within the Community Inversion Framework v1.1 to assimilate $\delta^{13}C(CH_4)$ and CH_4 : a case study with model LMDz-SACS

Joël Thanwerdas[1,*], Marielle Saunois[1], Antoine Berchet[1], Isabelle Pison[1], Bruce H. Vaughn[2], Sylvia Englund Michel[2], and Philippe Bousquet[1]

[1]Laboratoire des Sciences du Climat et de l'Environnement, CEA-CNRS-UVSQ, IPSL, Gif-sur-Yvette, France.
[2]INSTAAR - University of Colorado, Boulder, CO, United States

Correspondence: J. Thanwerdas (joel.thanwerdas@lsce.ipsl.fr)

Abstract.

Atmospheric ~~CH_4 mixing ratios~~ CH_4 mole fractions resumed their increase in 2007 after a plateau during the ~~period~~ 1999-2006 ~~, suggesting varying~~ period, indicating relative changes in the sources and sinks~~as main drivers~~. Estimating sources by exploiting observations within an inverse modeling framework (top-down approaches) is a powerful approach. It is nevertheless challenging to efficiently differentiate co-located emission categories and sinks by using ~~CH_4~~ CH_4 observations alone. As a result, top-down approaches are limited when it comes to fully understanding ~~CH_4~~ CH_4 burden changes and attribute these changes to specific source variations. ~~CH_4 source isotopic signatures~~ $\delta^{13}C(CH4)_{source}$ isotopic signatures of CH_4 sources differ between emission categories (biogenic, thermogenic and pyrogenic), and can therefore be used to address this limitation. Here, a new 3-D variational inverse modeling framework designed to assimilate ~~$\delta^{13}C(CH_4)$~~ $\delta^{13}C(CH_4)$ observations together with ~~CH_4~~ CH_4 observations is presented. This system is capable of optimizing both the emissions and associated source signatures of multiple emission categories at the pixel scale. To our knowledge, this represents the first attempt to carry out variational inversion assimilating $\delta^{13}C(CH_4)$ with a 3-D chemistry-transport model (CTM) and to independently optimize isotopic source signatures of multiple emission categories. We present the technical implementation of joint ~~CH_4 and $\delta^{13}C(CH_4)$~~ CH_4 and $\delta^{13}C(CH_4)$ constraints in a variational system, and analyze how sensitive the system is to the setup controlling the optimization using the ~~3-D Chemistry-Transport Model~~ LMDz-SACS 3-D CTM. We find that assimilating ~~$\delta^{13}C(CH_4)$~~ $\delta^{13}C(CH_4)$ observations and allowing the system to adjust ~~source isotopic~~ isotopic source signatures provide relatively large differences in global flux estimates for wetlands (~~5), microbial (6~~ -5.7 $TgCH_4.yr^{-1}$), agriculture and waste (-6.4 $TgCH_4.yr^{-1}$), fossil fuels (~~8~~ $+8.6$ $TgCH_4.yr^{-1}$) and biofuels-biomass burning (~~4~~ $+3.2$ $TgCH_4.yr^{-1}$) categories compared to the results inferred without assimilating ~~$\delta^{13}C(CH_4)$~~ $\delta^{13}C(CH_4)$ observations. More importantly, when assimilating both ~~CH_4 and $\delta^{13}C(CH_4)$~~ CH_4 and $\delta^{13}C(CH_4)$ observations, but assuming that the source signatures are perfectly known, ~~increase these differences between the system with CH_4 and the enhanced one with $\delta^{13}C(CH_4)$~~ these differences increase by a factor ~~3 or 4~~of 3-4, strengthening the importance of having as accurate ~~as possible signatures~~signature estimates as possible. Initial conditions, uncertainties ~~on $\delta^{13}C(CH_4)$~~ in $\delta^{13}C(CH_4)$ observations or the number of optimized categories have a much smaller impact (less than 2 $TgCH_4.yr^{-1}$).

1 Introduction

Methane (~~CH_4~~CH_4) is a powerful greenhouse gas and is responsible for 23 % (Etminan et al., 2016) of the radiative forcing induced by the well-mixed greenhouse gases (CO_2, ~~CH_4~~CH_4, N_2O). Atmospheric ~~CH_4 mixing ratios~~ CH_4 mole fractions have increased quasi-continuously since the pre-industrial era and by about 9 ~~ppb/yr~~ ppb.yr^{-1} from 1984 to 1998 ~~(www.esrl.noaa.gov/gmd/ccgg/trends_ch4/)~~(Dlugokencky, 2021). After a plateau between 1999 and 2006 that still generates attention and controversy (e.g., Fujita et al., 2020; Thompson et al., 2018; McNorton et al., 2018; Turner et al., 2017; Schaefer et al., 2016; Schwietzke et al., 2016; Rice et al., 2016), the ~~mixing ratios~~ mole fractions resumed their increase at a large rate, exceeding 10 ~~ppb/yr~~ ppb.yr^{-1} in 2014 and 2015. Trends in atmospheric ~~CH_4~~ CH_4 are caused by a small imbalance between large sources and sinks. Assessing their spatio-temporal characteristics is particularly challenging considering the variety of ~~methane~~ CH_4 emissions. Yet, identifying and quantifying the processes contributing to these changes is mandatory to formulate relevant ~~CH_4~~ CH_4 mitigation policies that would contribute to meet the target of the 2015 UN Paris Agreement on Climate Change and to limit climate warming to 2~~°C~~ °C.

Thanks to continuous efforts of surface monitoring networks, the spatial coverage and the accuracy of the atmospheric ~~methane~~ CH_4 measurements provided to the scientific community increased over the last decades. Consequently, top-down estimates using inversion methods emerged and became relevant, along with bottom-up estimates, to explain and quantify the recent sources and sinks variations. The first inverse modeling techniques were designed in the late 1980s and early 1990s for inferring greenhouse gas sources and sinks from atmospheric CO_2 measurements (Enting and Newsam, 1990; Newsam and Enting, 1988). ~~The~~ Without regularization of the problem, e.g. providing prior information, the inverse problem is ~~considered as "~~ill-conditioned (or ill-posed~~" (non-uniqueness of the solution, no continuity with the data) and therefore necessitates as many constraints as possible to be regularized. Several~~). It means that there is no unique solution to the problem but also that a small error in the assimilated data (here atmospheric observations) can result in large errors in the derived solution. Several inversion methods have been designed over the years, among which analytical (e.g., Bousquet et al., 2006; Gurney et al., 2002), ensemble (e.g., Zupanski et al., 2007; Peters et al., 2005) and variational methods (e.g., Chevallier et al., 2005). The variational formulation uses the adjoint equations of a specific model to compute the gradient of a cost function and then minimize it, for example using a gradient descent method. Computational times and memory costs do not scale with the number of measurements and the number of variables to control, contrary to the analytical and ensemble methods, which can hardly accommodate very large observational datasets and control vectors at the same time. Thus, the variational formulation is preferred to the others when optimizing emissions and sinks at the pixel scale using large volumes of observational data, although its main limitation is the numerical cost to access posterior uncertainties when there is non-linearity in the inversion problem (Berchet et al., 2021).

Inversion systems generally assimilate measurements from ground-based stations and/or satellites to constrain the global sources and sinks of ~~CH_4~~CH_4, starting from a prior knowledge of these. These systems are very effective to provide total emission estimates (e.g., Saunois et al., 2020; Bergamaschi et al., 2018, 2013; Saunois et al., 2017; Houweling et al., 2017, and references therein). However, differentiating the contributions of multiple co-located ~~CH_4~~ CH_4 source categories is challenging as it only relies on different seasonality cycles and on applied spatial distributions and error correlations (e.g., Bergamaschi et al., 2013, 2010). The atmospheric isotopic signal contains additional information on ~~methane~~ CH_4 emissions that can help to separate emission categories based on their source origin. The atmospheric isotopic signal ~~$\delta^{13}C(CH_4)$~~ $\delta^{13}\mathrm{C}(\mathrm{CH_4})$ is defined as:

$$\delta^{13}C(CH_4)\delta^{13}\mathrm{C}(\mathrm{CH_4}) = \frac{R}{R_{std}}\frac{R}{R_{\mathrm{std}}} - 1 \tag{1}$$

where R and R~~$_{std}$~~ $_{\mathrm{std}}$ denote the sample and standard ~~$^{13}CH_4$:$^{12}CH_4$~~ $^{13}\mathrm{CH_4}$:$^{12}\mathrm{CH_4}$ ratios. We use the ~~VPDB~~ Vienna - Pee Dee Belemnite (V-PDB) scale with R~~$_{std}$~~ $_{\mathrm{std}}$ = 0.00112372 (Craig, 1957) throughout this paper. ~~CH_4 source isotopic signatures $\delta^{13}C(CH_4)_{\mathrm{source}}$~~ The isotopic source signatures of CH_4, here denoted by $\delta^{13}\mathrm{C}(\mathrm{CH4})_{\mathrm{source}}$, notably differ between emission categories ranging from ^{13}C-depleted biogenic sources (~~approx. -62 ‰~~ -61.7 ± 6.2 ‰, one standard deviation) and thermogenic sources (~~approx. -44 ‰~~ -44.8 ± 10.7 ‰) to ^{13}C-enriched thermogenic sources (~~approx. -22 ‰) (Sherwood et al., 2017; Schwietzke et al., 2016)~~ -26.2 ± 4.8 ‰) (Sherwood et al., 2017; Schwietzke et al., 2016), although the distributions are very large and overlaps exist between the extreme values. Consequently, ~~$\delta^{13}C(CH_4)$~~ $\delta^{13}\mathrm{C}(\mathrm{CH_4})$ depends on both ~~the CH_4~~ CH_4 emissions and their isotopic signatures. Saunois et al. (2017) pointed out that many emission scenarios inferred from atmospheric inversions are not consistent with ~~$\delta^{13}C(CH_4)$~~ $\delta^{13}\mathrm{C}(\mathrm{CH_4})$ observations and that this ~~constrain~~ constraint must be integrated into the inversion systems to avoid such inconsistencies. In addition, they highlighted the sensitivity of the atmospheric isotopic signal to the source partitioning and prescribed isotopic ratios. Since the 1990s, ~~$\delta^{13}C(CH_4)$ have~~ $\delta^{13}\mathrm{C}(\mathrm{CH_4})$ has been monitored at multiple sites, ~~although less than for total CH_4,~~ providing opportunities to use this constraint within an inversion framework. In addition, these values have been shifting towards ~~smaller~~ more negative values since 2006 (Nisbet et al., 2019) when ~~CH_4~~ CH_4 trends resumed their increase, suggesting that this isotopic data can help to understand the processes that contributed to the ~~regrowth~~renewed growth. However, implementing the assimilation of such measurements into an inversion system is not straightforward and introduces additional complexity.

Hereinfafter, the assimilation of ~~$\delta^{13}C(CH_4)$~~ $\delta^{13}\mathrm{C}(\mathrm{CH_4})$ observations to constrain the estimates of an inversion is referred to as the "isotopic constraint". The implementation of such a constraint in an inversion system have already been attempted in previous studies focusing on ~~CH_4~~ CH_4 (e.g., Thompson et al., 2018; McNorton et al., 2018; Rigby et al., 2017; Rice et al., 2016; Schaefer et al., 2016; Schwietzke et al., 2016; Rigby et al., 2012; Neef et al., 2010; Bousquet et al., 2006; Fletcher et al., 2004) but, to our knowledge, never in a variational system associated to a 3-D chemistry-transport model (CTM). Adding this isotopic constraint to a variational inversion system is challenging as, in contrast to an analytic inversion in which the response functions of the model are precomputed, the isotopic constraints have to be considered both in the forward (simulated isotopic values) and the adjoint (sensitivity of isotopic observations to optimized variables) versions of the model.

This new system was implemented in the Community Inversion Framework (CIF), supported by the European Union H2020 project VERIFY (http://www.community-inversion.eu) and required to implement new forward, tangent-linear and adjoint operations. The forward operations were previously used to estimate the impact of the Cl sink on the modeling of CH_4 and $\delta^{13}\mathrm{C}(\mathrm{CH_4})$ in LMDz-SACS (Thanwerdas et al., 2019). The purpose of this study is to present the technical implementation of the isotopic constraint in a variational inversion system and to investigate the sensitivity of this new configuration to different parameters. Our aim is not to estimate trends in sectoral emissions over the last two decades : future studies will address the estimation of ~~CH_4 sources~~ CH_4 emissions over longer periods of time using this new system. The technical implementation and the various tested configurations are presented in Sect.~~2.~~ 2. We analyze the results in Sect.~~3.~~ 3. Sect.~~4~~ 4 presents our conclusions and recommendations on using such a multi-constraint variational system.

2 Methods

2.1 Theory of variational inversion

The notations introduced here follow the convention defined by Ide et al. (1997) and Rayner et al. (2019). The observation vector is called $\mathbf{y}^{\mathrm{o}}$. It includes here all available observations, namely ~~CH_4 and $\delta^{13}C(CH_4)$~~ CH_4 and $\delta^{13}\mathrm{C}(\mathrm{CH}_4)$ measurements retrieved by surface stations, over the full simulation time-window (see Sect.~~2.4.2~~ 2.4.2). The associated errors are assumed to be unbiased and Gaussian and are described within the error covariance matrix $\mathbf{R}$. This matrix accounts for all errors contributing to mismatches between simulated and observed values. $\mathbf{x}$ is the control vector and includes all the variables (here ~~CH_4~~ CH_4 surface fluxes, initial ~~CH_4 mixing ratios~~CH_4 mole fractions, source signatures ~~$\delta^{13}C(CH_4)_{\mathrm{source}}$ and initial $\delta^{13}C(CH_4)$~~ $\delta^{13}\mathrm{C}(\mathrm{CH4})_{\mathrm{source}}$ and initial $\delta^{13}\mathrm{C}(\mathrm{CH}_4)$ values) optimized by the inversion system. Hereinafter, these variables will be referred to as the "control variables". Prior information about the control variables are provided by the vector $\mathbf{x}^{\mathrm{b}}$. Its associated errors are also assumed to be unbiased and Gaussian and are described within the error covariance matrix $\mathbf{B}$. $\mathcal{H}$ is the observation operator that projects the control vector $\mathbf{x}$ into the observation space. This operator mainly consists of the 3-D ~~Chemistry-Transport Model (CTM)~~ CTM (here LMDz-SACS introduced in Sect ~~2.2~~ 2.2). Nevertheless, the CTM is followed by spatial and time operators, which interpolate the simulated fields to produce simulated equivalents of the assimilated observations at specific locations and times, making the simulations and observations comparable. An additional 'transformation' operator, implemented in the new system, enables comparison between distinct simulated tracers, e.g.~~$^{12}CH_4$ and $^{13}CH_4$~~, $^{12}\mathrm{CH}_4$ and $^{13}\mathrm{CH}_4$, and observations, e.g.~~$\delta^{13}C(CH_4)$~~ , $\delta^{13}\mathrm{C}(\mathrm{CH}_4)$ (see Sect~~2.3~~ 2.3).

In a variational formulation of the inference problem that allows for $\mathcal{H}$ non-linearity, the cost function J is defined as :

$$J(\mathbf{x}) = \frac{1}{2}(\mathbf{x}-\mathbf{x}^{\mathrm{b}})^{\mathrm{T}}\mathbf{B}^{-1}(\mathbf{x}-\mathbf{x}^{\mathrm{b}}) + \frac{1}{2}(\mathcal{H}(\mathbf{x})-\mathbf{y}^{\mathrm{o}})^{\cancel{T}\mathrm{T}}\mathbf{R}^{-1}(\mathcal{H}(\mathbf{x})-\mathbf{y}^{\mathrm{o}}) \quad (2)$$

$$= J_b(\mathbf{x}) + J_o(\mathbf{x}) \quad (3)$$

The cost function is therefore a sum of two parts :

- The first part is induced by the differences between the posterior and prior variables (J_b).
- The second is induced by the differences between simulations and observations (J_o)

The minimum of J can be reached iteratively with a descent algorithm that requires several computations of the gradient of J with respect to the control vector $\mathbf{x}$:

$$\nabla J_{\mathbf{x}} = \mathbf{B}^{-1}(\mathbf{x}-\mathbf{x}^{\mathrm{b}}) + \mathcal{H}^{*}(\mathbf{R}^{-1}(\mathcal{H}(\mathbf{x})-\mathbf{y}^{\mathrm{o}})) \quad (4)$$

$\mathcal{H}^*$ denotes the adjoint operator of $\mathcal{H}$. ~~Although the variational method is a powerful approach for dealing with large numbers of observations and control variables (several hundred thousands), it implies~~ As in analytical and ensemble methods, the variational formulation necessitates the inversion of both error matrices $\mathbf{R}$ and $\mathbf{B}$. In most applications, ~~R~~ $\mathbf{R}$ is considered diagonal as point observations are distant in time and space ~~, allowing inversing it~~ (i.e., uncorrelated observation errors), allowing for the inverse to be calculated easily, although that assumption ~~may change~~ should be revised with the increasing availability of satellite sources (Liu et al., 2020). B is rarely diagonal due to spatial and temporal correlations of errors in the fluxes. However, B is often decomposed as combinations of smaller matrices, e.g., using Kronecker products of sub-correlation matrices, which allows to compute its inverse by blocks.

2.2 The Chemistry-Transport Model

The LMDz ~~General Circulation Model~~ general circulation model (GCM) is the atmospheric component of the Institut Pierre-Simon Laplace Coupled Model (IPSL-CM) developed at the Laboratoire de Météorologie Dynamique (LMD) (Hourdin et al., 2006). The version of LMDz we use is an 'offline' version dedicated to the inversion framework created by Chevallier et al. (2005): precomputed air mass fluxes provided by the online version of LMDz are given as inputs to the transport model, reducing significantly the computational time. The model is set up at a horizontal resolution of 3.8° ~~x~~ × 1.9° (96 grid cells in longitude and latitude) with 39 hybrid sigma-pressure levels reaching an altitude up to about 75 km. About 20 levels are dedicated to the stratosphere and the mesosphere. The model time-step is 30 min and the output ~~mixing ratios~~ mole fractions are 3-hourly snapshots. The horizontal winds are nudged towards ECMWF meteorological analyses (ERA-Interim) in the online version of the model then fed to the offline version. Vertical diffusion is parameterized by a local approach from Louis (1979), and deep convection processes are parameterized by the Tiedtke (1989) scheme.

The offline model LMDz is coupled with the Simplified Atmospheric Chemistry System (SACS) (Pison et al., 2009). This chemistry system was previously used to simulate the oxidation chain of hydrocarbons, including ~~CH_4~~ CH_4, formaldehyde (CH_2O), carbon monoxide (CO) and molecular hydrogen (H_2)~~together with methyl chloroform (MCF)~~. For the purpose of this study, this system ~~has been~~ was converted into a chemistry parsing system. It follows the same principle as the one used by the regional model CHIMERE (Menut et al., 2013) and therefore allows for user-specific chemistry reactions. As a result, it generalizes the previous SACS module to any possible set of reactions. The adjoint code has also been implemented to allow variational inverse ~~modelling~~modeling. The different species are either prescribed (here OH, $O(^1D)$ and Cl) or simulated (here ~~$^{12}CH_4$ and $^{13}CH_4$~~ $^{12}CH_4$ and $^{13}CH_4$). The prescribed species are not transported in LMDz, nor are their ~~mixing ratios~~ mole fractions updated through chemical production or destruction. Such species are only used to calculate reaction rates to update simulated species at each model time step. In this study, the isotopologues ~~$^{12}CH_4$ and $^{13}CH_4$~~ $^{12}CH_4$ and $^{13}CH_4$ are simulated as separate tracers and ~~CH_4~~ CH_4 is defined as the sum of both isotopologues. Cl + ~~CH_4 oxidation has been~~ CH_4 oxidation was implemented to complete the chemical removal of ~~CH_4~~ CH_4, which previously only accounted for OH + ~~CH_4~~ CH_4 and $O(^1D)$ + ~~CH_4~~ CH_4 in the SACS scheme. ~~Fractionation values (KIE for~~

In the atmosphere, radicals (OH, $O(^1D)$ or Cl) react faster with $^{12}CH_4$ than with $^{13}CH_4$. This effect is called the Kinetic Isotope Effect ~~)~~ (KIE) or the fractionation effect. Fractionation values are prescribed to the different sinks in SACS. Here, ~~KIE~~

this value is defined by $\mathrm{KIE} = k_{12}/k_{13}$ where k_{12} is the ~~constant rate of the reaction involving $^{12}CH_4$ and~~ rate constant of a reaction between a radical and $^{12}CH_4$. k_{13} is the ~~constant rate of the same reaction involving $^{13}CH_4$~~rate constant of the reaction between the same radical and $^{13}CH_4$. Additional information ~~is~~ and prescribed KIE values are provided in the supplement (Text S2).

The chemistry-transport LMDz-SACS is used to test the new variational inverse ~~modelling~~ modeling system that is described in the next section.

2.3 Technical implementation of the isotopic constraint

The isotopic ~~multi-constrain~~ multi-constraint system was implemented in the ~~Community Inversion Framework (CIF), supported by the European Union H2020 project VERIFY (http://www.community-inversion.eu)~~CIF. The CIF has been designed to allow comparison of different approaches, models and inversion systems used in the inversion community ~~(Berchet et al., 2020)~~(Berchet et al., 2021). Different atmospheric transport models, regional and global, Eulerian and Lagrangian are implemented within the CIF. The system presented in this paper has been originally designed to run and be tested with LMDz-SACS but can theoretically be coupled with all models implemented in the CIF framework. The system is able to :

- Assimilate ~~$\delta^{13}C(CH_4)$ and CH_4~~ $\delta^{13}\mathrm{C}(\mathrm{CH_4})$ and $\mathrm{CH_4}$ observations together.
- Independently optimize fluxes and isotopic signatures for multiple emission categories.
- Optimize ~~$\delta^{13}C(CH_4)$ and CH_4~~ $\delta^{13}\mathrm{C}(\mathrm{CH_4})$ and $\mathrm{CH_4}$ initial conditions.

Figure~~1~~ 1 shows the different steps of a minimization iteration of the cost function. Each iteration performed with the descent algorithm can be decomposed into four main steps presented below. For clarity, we only present here the optimization of ~~CH_4~~ $\mathrm{CH_4}$ fluxes and associated source signatures but ~~CH_4 and $\delta^{13}C(CH_4)$~~ $\mathrm{CH_4}$ and $\delta^{13}\mathrm{C}(\mathrm{CH_4})$ initial conditions can also be optimized by the system following the same process.

1. The process starts with a forward run. The different flux variables are extracted and converted into ~~$^{12}CH_4$ and $^{13}CH_4$~~ $^{12}\mathrm{CH_4}$ and $^{13}\mathrm{CH_4}$ mass fluxes for each category following the Eq.~~(5)-(7) below.~~ 5 and 6 below.

$$\cancel{A^i = (1+\delta^{13}C(CH_4)^i_{\mathrm{source}})\cdot R_{std}}\, F^i_{12} = \cancel{\frac{M_{12}}{M_{TOT}}}\,\frac{M_{12}}{M_T}\cdot\frac{1}{1+A^i}\cdot F_{\cancel{TOT}T}{}^i \tag{5}$$

$$F^i_{13} = \cancel{\frac{M_{13}}{M_{TOT}}}\,\frac{M_{13}}{M_T}\cdot\frac{A^i}{1+A^i}\cdot F_{\cancel{TOT}T}{}^i \tag{6}$$

with

$$A^i = (1+\delta^{13}\mathrm{C}(\mathrm{CH4})^{\mathrm{i}}_{\mathrm{source}})\cdot R_{\mathrm{std}} \tag{7}$$

~~F^i_{TOT}~~F^i_T, F^i_{12} and F^i_{13} are the ~~CH_4, $^{12}CH_4$ and $^{13}CH_4$ fluxes in~~ CH_4, $^{12}CH_4$ and $^{13}CH_4$ mass fluxes of a specific category i, respectively. ~~M_{TOT}~~M_T, M_{12} and M_{13} are the ~~CH_4, $^{12}CH_4$ and $^{13}CH_4$~~ CH_4, $^{12}CH_4$ and $^{13}CH_4$ molar masses, respectively. ~~$\delta^{13}C(CH_4)$~~$\delta^{13}C(CH_4)^i_{source}$ is the ~~source~~ isotopic signature of the category i. M_T should preferably depend on M_{12} and M_{13} when converting the mass fluxes:

$$M_T = \frac{M_{12} + A^i \cdot M_{13}}{1 + A^i} \tag{8}$$

However, the complexity of the forward, tangent-linear and adjoint codes would be largely enhanced by such a relationship. The code structure would also be less generic, i.e., it could not be used for a joint assimilation of multiple isotopologues of CH_4, such as both $\delta^{13}C(CH_4)$ and $\delta D(CH_4)$. We choose to implement M_T as a constant that can be prescribed freely by the user, therefore without considering any influence of the M_{12} and M_{13} values, also prescribed by the user. As the observed isotopic source signatures roughly vary between -70 ‰ and -10 ‰, a maximum variation of 0.004 % in M_T could be expected. It will very likely not affect the results of our study or that of any other inversion performed with our system.

The ~~$^{12}CH_4$ and $^{13}CH_4$~~ $^{12}CH_4$ and $^{13}CH_4$ total fluxes are then ~~provided~~ calculated by summing all categories and used by the model LMDz-SACS to simulate the ~~$^{12}CH_4$ and $^{13}CH_4$ atmospheric mixing ratios~~ $^{12}CH_4$ and $^{13}CH_4$ atmospheric mole fractions over the time-window considered. ~~Finally~~After the simulation, the simulated values are converted ~~back to CH_4 and $\delta^{13}C(CH_4)$~~ to CH_4 and $\delta^{13}C(CH_4)$ simulated equivalent of the assimilated observations using Eq.~~(8) and(9) below :~~ 9 and 10 below :

$$[\cancel{CH_4}\mathrm{CH_4}] = [\cancel{^{12}CH_4}{}^{12}\mathrm{CH_4}] + [\cancel{^{13}CH_4}{}^{13}\mathrm{CH_4}] \tag{9}$$

$$\cancel{\delta^{13}C(CH_4)}\delta^{13}\mathrm{C(CH_4)} = \cancel{\frac{[^{13}CH_4]}{[^{12}CH_4]}}\frac{[^{13}\mathrm{CH_4}]}{[^{12}\mathrm{CH_4}]} \cdot \cancel{\frac{1}{R_{std}}}\frac{1}{R_{\mathrm{std}}} - 1 \tag{10}$$

~~$[CH_4]$, $[^{12}CH_4]$ and $[^{13}CH_4]$ are CH_4, $^{12}CH_4$ and $^{13}CH_4$ atmospheric mixing ratios~~ $[CH_4]$, $[^{12}CH_4]$ and $[^{13}CH_4]$ are CH_4, $^{12}CH_4$ and $^{13}CH_4$ atmospheric mole fractions simulated by the model in $\mathrm{mol\,mol^{-1}}$, respectively.

2. These simulated values are then compared to the available observations in order to compute ~~$\mathcal{H}(\mathbf{x}) - \mathbf{y}^o$~~ $\mathcal{H}(\mathbf{x}) - \mathbf{y}^o$ which is further used to infer the cost function and generate ~~CH_4 and $\delta^{13}C(CH_4)$~~ CH_4 and $\delta^{13}C(CH_4)$ adjoint forcings (indicated by the "*" star superscript symbol) that compose the vector $\delta\mathbf{y}^*$:

$$\delta\mathbf{y}^* = \mathbf{R}^{-1}(\mathcal{H}(\mathbf{x}) - \mathbf{y}^o) \tag{11}$$

~~This~~ Although this vector is normally used directly as input to the adjoint model (see Eq.~~4)but in the new system, the adjoint forcings CH_4~~ 4), the CH_4 and ~~$^{13}C(CH_4)$~~ $\delta^{13}C(CH_4)$ adjoint forcings must first be converted into the ~~adjoint forcings $^{12}CH_4$~~ $^{12}CH_4$ and ~~$^{13}CH_4$~~ $^{13}CH_4$ adjoint forcings in the new system.

3. The newly designed adjoint code that converts ~~CH_4 and $\delta^{13}C(CH_4)$~~ $\mathrm{CH_4}$ and $\delta^{13}\mathrm{C(CH_4)}$ adjoint forcings into ~~$^{12}CH_4$ and $^{13}CH_4$~~ $^{12}\mathrm{CH_4}$ and $^{13}\mathrm{CH_4}$ adjoint forcings is based on the Eq.~~(11)-(13)~~ 12, 13 and 14 depending on the type of the initial observation.

$$[{}^{12}CH_4\,{}^{12}\mathrm{CH_4}]^*_{CH_4\,\mathrm{CH_4}} = [{}^{13}CH_4\,{}^{13}\mathrm{CH_4}]^*_{CH_4\,\mathrm{CH_4}} = [CH_4\,\mathrm{CH_4}]^* \tag{12}$$

$$[{}^{12}CH_4\,{}^{12}\mathrm{CH_4}]^*_{\delta^{13}C\,\delta^{13}\mathrm{C}} = -\frac{[{}^{13}CH_4]}{[{}^{12}CH_4]^2}\frac{[{}^{13}\mathrm{CH_4}]}{[{}^{12}\mathrm{CH_4}]^2}\cdot\frac{1}{R_{std}}\frac{1}{R_{\mathrm{std}}}\cdot\delta^{13}C(CH_4)\,\delta^{13}\mathrm{C(CH_4)}^* \tag{13}$$

$$[{}^{13}CH_4\,{}^{13}\mathrm{CH_4}]^*_{\delta^{13}C\,\delta^{13}\mathrm{C}} = \frac{1}{[{}^{12}CH_4]}\frac{1}{[{}^{12}\mathrm{CH_4}]}\cdot\frac{1}{R_{std}}\frac{1}{R_{\mathrm{std}}}\cdot\delta^{13}C(CH_4)\,\delta^{13}\mathrm{C(CH_4)}^* \tag{14}$$

~~$[^{12}CH_4]^*_{CH_4}$ and $[^{13}CH_4]^*_{CH_4}$~~ $[^{12}\mathrm{CH_4}]^*_{\mathrm{CH_4}}$ and $[^{13}\mathrm{CH_4}]^*_{\mathrm{CH_4}}$ are adjoint forcings associated with ~~CH_4 observations. $[^{12}CH_4]^*_{\delta^{13}C}$ and $[^{13}CH_4]^*_{\delta^{13}C}$~~ $\mathrm{CH_4}$ observations. $[^{12}\mathrm{CH_4}]^*_{\delta^{13}\mathrm{C}}$ and $[^{13}\mathrm{CH_4}]^*_{\delta^{13}\mathrm{C}}$ are adjoint forcings associated with ~~$\delta^{13}C(CH_4)$~~ $\delta^{13}\mathrm{C(CH_4)}$ observations. The adjoint code of the CTM is then run with these adjoint forcings as inputs.

Outputs of the adjoint run provide the sensitivities of the adjoint forcings to the ~~$^{12}CH_4$ and $^{13}CH_4$~~ $^{12}\mathrm{CH_4}$ and $^{13}\mathrm{CH_4}$ mass fluxes of a specific category i~~denoted~~ , denoted by $F^{*,i}_{12}$ and $F^{*,i}_{13}$. Equations~~(14) and(15)~~ 15 and 16 convert them back to sensitivities to the initial control variables, denoted ~~$F^{*,i}_{TOT}$ and $\delta^{13}C(CH_4)^{*,i}_{\mathrm{source}}$.~~ by $F^{*,i}_{T}$ and $\delta^{13}\mathrm{C(CH4)_{source}}^{*,i}$.

$$F_{TOT\,T}{}^{*,i} = \frac{1}{1+A}\cdot\left[\frac{M_{12}}{M_{TOT}}\frac{M_{12}}{M_T}\cdot F^{*,i}_{12} + \frac{M_{13}}{M_{TOT}}\frac{M_{13}}{M_T}\cdot A\cdot F^{*,i}_{13}\right] \tag{15}$$

$$\delta^{13}C(CH_4)^{*,i}_{\mathrm{source}}\,\delta^{13}\mathrm{C(CH4)}^{*,\mathrm{i}}_{\mathrm{source}} = R_{std\,\mathrm{std}}\cdot\frac{F_{TOT}}{(1+A)^2}\frac{F_T}{(1+A)^2}\cdot\left[\frac{M_{13}}{M_{TOT}}\frac{M_{13}}{M_T}\cdot F^{*,i}_{13} - \frac{M_{12}}{M_{TOT}}\frac{M_{12}}{M_T}\cdot F^{*,i}_{12}\right] \tag{16}$$

4. The minimization algorithm ~~uses~~ utilizes these sensitivities to compute the gradient of the cost function. It then finds an optimized control vector ~~that reduces~~ reducing the cost function and ~~that is~~ used for the next iteration.

In order to confirm that the several adjoint operations have been correctly implemented, we also provide the results of multiple adjoint tests in the supplement (Text S4).

2.4 Setup of the reference simulation

The reference configuration (REF) is a variational inversion that optimizes the ~~CH_4~~ $\mathrm{CH_4}$ emission fluxes and ~~$\delta^{13}C(CH_4)$ source isotopic~~ $\delta^{13}\mathrm{C(CH_4)}$ isotopic source signatures of five different categories ~~(:~~: biofuels-biomass burning ~~, microbial~~(BB), agriculture and waste (AGW), fossil fuels ~~, natural and wetlands)~~ (FF), wetlands (WET) and other natural sources (NAT). $\mathrm{CH_4}$ and ~~the CH_4/$\delta^{13}C(CH_4)$initial conditions~~$\delta^{13}\mathrm{C(CH_4)}$ initial conditions are also optimized. The assimilation time-window is the ~~period~~ 2012-2017 period. The five categories originate from an aggregation of ten sub-categories (~~Table 1) and~~ see Table 1) and are chosen to be as isotopically consistent as possible. Sinks are not optimized here.

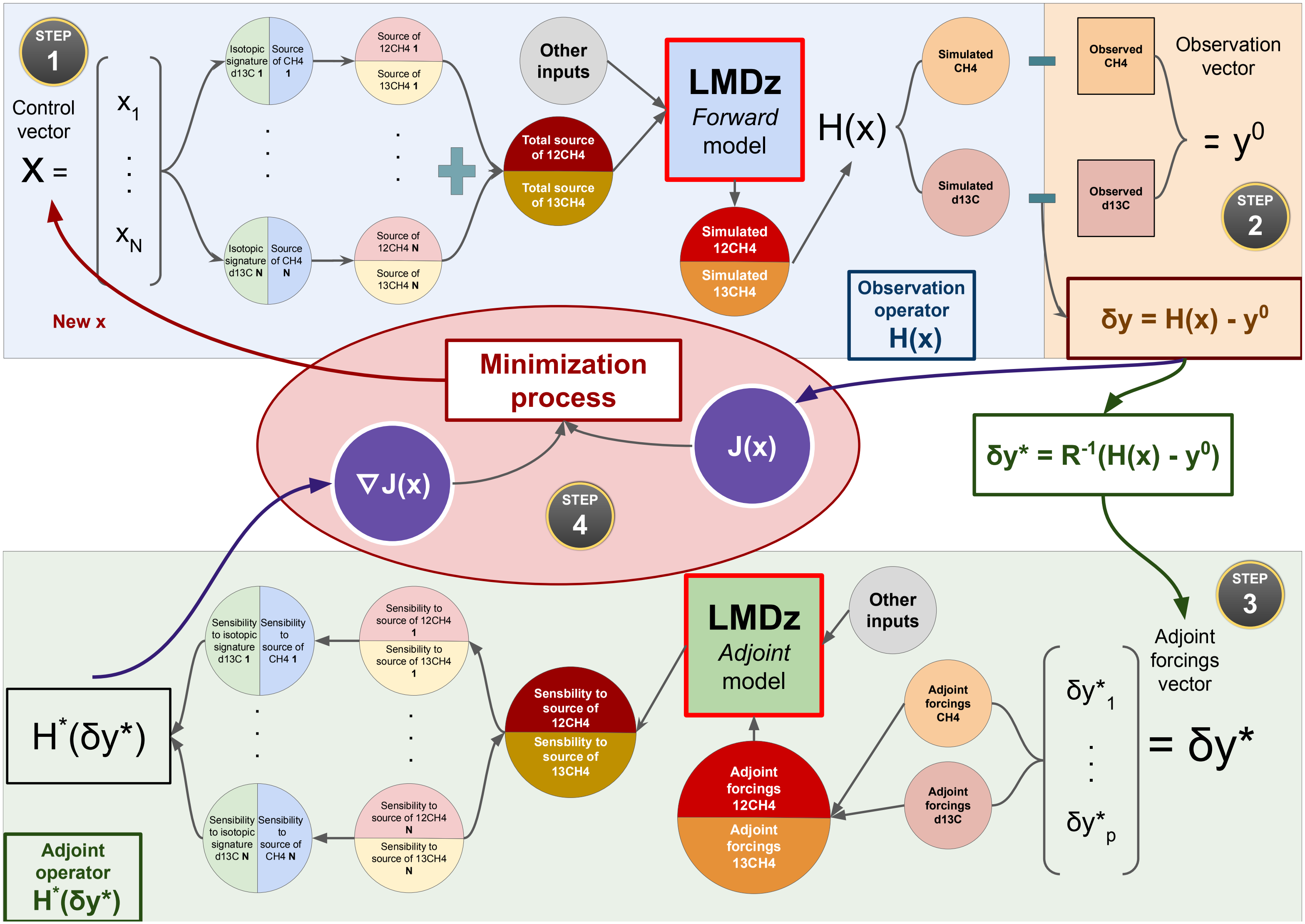

Figure 1. The minimization iteration process in the newly designed system.~~The~~

]The minimization iteration process in the newly designed system. The "step" ~~black circles with gold border indicates the reading direction to follow. Step~~ black circles with a gold border indicates the reading direction to follow. Step 1 ~~(blue rectangle) refers to a forward run. Step~~ (blue rectangle) refers to a forward run. Step 2 ~~(orange rectangle) refers to the forward and adjoint operations required to compare observations and simulated values. Step~~ (orange rectangle) refers to the forward and adjoint operations required to compare observations and simulated values. Step 3 ~~(green rectangle) refers to an adjoint run. This step must be read from the right to the left. Step~~ (green rectangle) refers to an adjoint run. This step must be read from the right to the left. Step 4 ~~(red ellipse) refers to the minimization of the cost function operated by the dedicated minimization algorithm. Note that results of Step~~ (red ellipse) refers to the minimization of the cost function operated by the dedicated minimization algorithm. Note that results of Step 2 ~~are used both in the minimization process (red ellipse) and as inputs for Step~~ are used both in the minimization process (red ellipse) and as inputs for Step 3. ~~The minimization iteration process followed by the previous system is also illustrated in the supplement (Fig.~~ The minimization iteration process followed by the previous system is also illustrated in the supplement (Fig. S1)

Table 1. Emissions and flux-weighted isotopic signatures of the ~~CH_4~~ CH_4 sources averaged over 2012-2017 for different categories and their sub-categories. Prior uncertainties in fluxes are set to 100 % for all categories and sub-categories. * Unc. : Prior uncertainty in the isotopic signature prescribed to the category or the sub-category as a percentage of the signature. ~~Prior uncertainty in fluxes are set to 100 % for all categories and sub-categories~~CH19 : Chang et al. (2019) ; GA18 : Ganesan et al. (2018) ; SH17 : Sherwood et al. (2017) ; WA16 : Warwick et al. (2016) ; ZA16 : Zazzeri et al. (2016) ; TO12 : Townsend-Small et al. (2012) ; KL10 : Klevenhusen et al. (2010) ; BO06 : Bousquet et al. (2006) ; BR01 : Bréas et al. (2001) ; SA01 : Sansone et al. (2001) ; CH00 : Chanton et al. (2000) ; HO00 : Holmes et al. (2000) ; CH99 : Chanton et al. (1999) ; BE98 : Bergamaschi et al. (1998) ; LE93 : Levin et al. (1993).

Categories	Emissions ($Tg.yr^{-1}$)	Signature (‰)	Unc.* (%)	Sub-categories	Emissions ($Tg.yr^{-1}$)	Signature (‰)	Unc.* (%)	Signature references
WET	180.3	-60.8	20	Wetlands	180.3	-60.8	20	GA18
AGW	226.4	-59.1	20	Rice cultivation	38.0	-63	20	SH17 ; BO06 ; BR01
				Livestock	117.8	-63.6	20	CH19
				Waste	70.6	-49.5	20	KL10 ; TO12 ; CH99 ; BE98 ; LE93
FF	116.3	-43.4	25	Coal	38.4	-40.4	25	SH17 ; ZA16
				Oil, Gas, Industry	77.9	-44.9	25	SH17
BB	28.4	-22.5	40	Biofuels-biomass burning	28.4	-22.5	40	BO06 ; CH00
NAT	38.1	-49.9	15	Oceanic sources	14.4	-42.0	20	BR01 ; HO00 ; SA01
				Termites	8.7	-63.0	20	TH18 ; SH17 ; WA16
				Geological (onshore)	15.0	-50.0	20	BO06
Total	589.5	-54.1		Total	589.5	-54.1		

2.4.1 Control vector x and B matrix

We adopt the ~~CH_4~~ CH_4 emissions compiled for inversions performed as part of the Global Methane Budget (Saunois et al., 2020). Anthropogenic (including biofuels) and ~~fire~~ biomass burning emissions are based on the ~~EDGARv432 database ()~~ EDGARv4.3.2 database (Janssens-Maenhout et al., 2017) and the GFED4s databases (van der Werf et al., 2017), respectively. Statistics from British Petroleum (BP) and the Food and Agriculture Organization of the United Nations (FAO) have been used to extend the ~~EDGARv432~~ EDGARv4.3.2 database, ending 2012, until 2017. The natural sources emissions are based on averaged literature values : Poulter et al. (2017) for wetlands, Kirschke et al. (2013) for termites, Lambert and Schmidt (1993) for ~~ocean~~ oceanic sources and Etiope (2015) for geological ~~sources. Globally averaged~~ (onshore) sources. Emissions from geological sources have been scaled down to 15 $TgCH_4.yr^{-1}$ in the prior emissions adopted in Saunois et al. (2020). All prior fluxes are prescribed at monthly resolution and at the spatial resolution of LMDz. Globally-averaged emissions over the ~~period~~ 2012-2017 period are listed in Table~~1.~~ 1.

~~Source isotopic~~ Prior estimates of isotopic source signatures are provided either at the pixel scale (for wetlands), at the regional scale based on TransCom regions (Patra et al., 2011) or at the global scale. The wetlands signature map is taken from Ganesan et al. (2018). Livestock ~~source isotopic~~ isotopic source signatures are taken from Chang et al. (2019) and aggregated into the 11-regions map by selecting region-specific values. ~~These~~ Livestock source signatures have been likely decreasing over time since the 1990s due to changes in C3/C4 diet within the major livestock producing countries and therefore annual values are prescribed. However, these estimates end in 2013 ~~, therefore~~ and we set the years 2014 to 2017 ~~are set~~ equal to the year 2013. Consequently, only the year 2012 has a different prescribed value from the other years. Coal and Oil, Gas, Industry (OGI) isotopic signature values are inferred from Sherwood et al. (2017) and Zazzeri et al. (2016) and aggregated into the same 11-regions map. The EDGARv4.3.2 categories PRO_OIL and PRO_GAS (fugitive emissions during oil and gas exploitation) largely contribute (∼90 %) to the total of the "Oil, Gas & Industry" sub-category. Therefore, we chose to neglect the influence of other subsub-categories (such as industry) on the isotopic signature of the category. As for the biofuels-biomass burning category, we use region-specific signatures over 11 regions. A global signature value is prescribed for each of the other categories. Except for the livestock category, all prior signatures are set constant over time. To infer the $\delta^{13}\mathrm{C(CH4)}_{\mathrm{source}}$ map of a category based on the sub-categories, the $^{12}\mathrm{CH}_4$ and $^{13}\mathrm{CH}_4$ fluxes for each emission sub-category within a category are derived based on Eq. 5 and 6 and added up. The resulting fluxes are then converted back to a $\delta^{13}\mathrm{C(CH4)}_{\mathrm{source}}$ map representing the aggregated isotopic signature of the category. Additional information regarding the chosen isotopic signatures and their references is provided in the supplement (Text S1).

Three values per month (10 days, 10 days and the rest) for ~~the~~ fluxes and their associated isotopic signatures are included in the control variables. Although the time variations of isotopic signatures are poorly constrained in the literature, we choose to include the same number of variables for fluxes and isotopic signatures in order to illustrate the full capabilities of the system and have it ready when more isotopic constraints will appear.

The portion of the diagonal of $\mathbf{B}$ associated to prior ~~CH_4~~ CH_4 emission fluxes is filled in with the variances set to 100 % of the square of the maximum of emissions over the cell and its eight neighbours during each month. Off diagonal terms of $\mathbf{B}$ (covariances) are based on correlation e-folding lengths (500 km over land and 1000 km over sea). The same method is applied for ~~source isotopic~~ isotopic source signatures, although a specific percentage of uncertainties deduced from the global values of Sherwood et al. (2017) is used to infer each category diagonal term (see Table~~1~~ 1). No temporal correlations are considered here. Finally, prior uncertainties ~~on~~ in initial conditions are set to 10~~% for CH_4~~ % for CH_4 (∼ 180 ppb) and 3~~% for $\delta^{13}\mathrm{C}(\mathrm{CH}_4)$~~ % for $\delta^{13}\mathrm{C}(\mathrm{CH}_4)$ (∼ 1.4 ‰).

2.4.2 Observation vector $\mathbf{y}$ and $\mathbf{R}$ matrix

~~CH_4~~ CH_4 observations are taken from the data archived at the World Data Centre for Greenhouse Gases (WDCGG) of the WMO Global Atmospheric Watch (WMO-GAW) program. We selected 66 stations from 13 surface monitoring networks providing in-situ measurements of ~~CH_4 mixing ratios~~ CH_4 mole fractions. The stations are displayed in Fig.~~2. Table S3 in the supplement provides a list of these 66 stations and specific information~~ 2.

~~$\delta^{13}\mathrm{C}(\mathrm{CH}_4)$~~ $\delta^{13}\mathrm{C}(\mathrm{CH}_4)$ observations are taken from 18 surface stations from the Global Greenhouse Gas Reference Network (GGGRN), part of the NOAA-ESRL~~Global Monitoring Division (NOAA-ESRL GMD~~'s Global Monitoring Laboratory (NOAA GML). Air samples ~~have been~~ were collected on an approximately weekly basis during the 2012-2017 period and analyzed by the Institute of Arctic and Alpine Research (INSTAAR) to provide ~~$\delta^{13}\mathrm{C}(\mathrm{CH}_4)$~~ $\delta^{13}\mathrm{C}(\mathrm{CH}_4)$ isotope ratio measurements. The analytical uncertainty of the isotopic measurements, based on a surveillance cylinder, is 0.06~~‰. Table S4 in~~

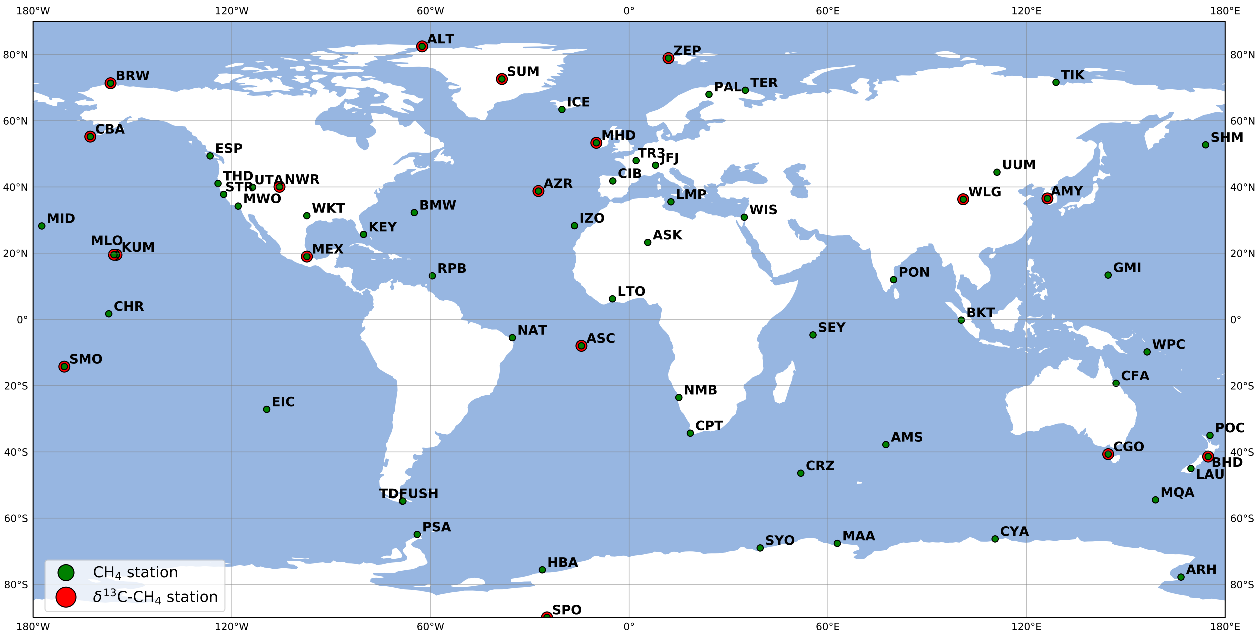

Figure 2. Locations of ~~CH_4~~ CH_4 and ~~$\delta^{13}C(CH_4)$~~ $\delta^{13}C(CH_4)$ surface stations. Affiliated networks are not displayed. More information can be found in the supplement (Table S3 and S4).

~~the supplement provides a list of these 18 stations and specific information.The observed high-frequency temporal variability cannot be adequately reproduced by the LMDz-SACS model.Therefore, instead of assimilating the real observations, we used a smooth~~ ‰. In this study, we focused on estimating monthly and annual flux variations rather than investigating daily or weekly variations. Prescribing error correlations in the $\mathbf{R}$ matrix (introduced in Sect. 2.1) can be used to ensure that the inversion preferentially constrains the components we are interested in (i.e., long-term trend and seasonal cycle). In order to keep the R matrix diagonal and to focus on monthly and annual variations of the signal, we chose to use $\delta^{13}C(CH_4)$ observational data based on a curve fitting the ~~real~~ original $\delta^{13}C(CH_4)$ observations. The fitting curve is a function including 3 polynomial parameters (quadratic) and 8 harmonic parameters as in Masarie and Tans (1995). After the fitting, the pseudo-observations were sampled at the same time as the original observations. We also hypothesized that the convergence would be slightly faster if a smooth curve fitting the real observations was used instead of the real observations, which appeared to be false (see Sect. 3.1). One sensitivity inversion aims at estimating the error introduced by this simplification (simulation S2 in Table~~2~~ 2).

The $\mathbf{R}$ matrix ~~introduced in Sect. 2.1~~ for both CH_4 and $\delta^{13}C(CH_4)$ is defined as diagonal, assuming that observation errors are not correlated, neither in space nor in time. This diagonal matrix can be decomposed into two parts : measurement and model error ~~variance~~variances. Measurement errors account for instrumental errors ~~while~~ whereas model errors encompass transport and representativity errors induced by the model :

$$\mathbf{R} = \mathbf{R}_{\mathbf{measurement}} + \mathbf{R}_{\mathbf{model}} \tag{17}$$

Here, we use the provided observation errors to fill the $\mathbf{R_{measurement}}$ diagonal matrix. Globalview-CH_4 ~~(Globalview-CH$_4$, 2009)~~ (GLOBALVIEW-CH4, 2009) values are used to represent model errors and prescribe variances at each station for ~~CH$_4$~~ CH_4 mixing ratio measurements in order to fill the $\mathbf{R_{model}}$ diagonal matrix. This simple approach has been used previously in atmospheric inversions (Locatelli et al., 2015, 2013; Yver et al., 2011; Bousquet et al., 2006; Rodenbeck et al., 2003). Errors in Globalview-CH_4 are computed at each site as the Root-Mean-Square-Error (RMSE) of the measurements on a smooth curve fitting them. As Globalview-CH_4 does not provide errors for ~~δ^{13}C(CH~~Globalview-CH_4 ~~)~~ measurements, the same method has been applied here. RMSE of the measurements on a smooth curve fitting them over the ~~period~~ 2012-2017 period is prescribed as the standard deviation for each site providing ~~δ^{13}C(CH$_4$)measurements~~ $\delta^{13}\mathrm{C(CH_4)}$ measurements. These errors range between 3-19 ppb for CH_4 observations and 0.11-0.20 ‰ for $\delta^{13}\mathrm{C(CH_4)}$ observations. Mean prescribed errors for each station are provided in the supplement (Tables S3 and S4).

2.4.3 Spin-up

~~The~~ Before starting the inversion, the model has been spun-up during 30 years using constant emissions and recycling meteorology from the year 2012 in order to consider the long timescales for isotopic changes (Tans, 1997). At the end of the spin-up, ~~δ^{13}C(CH$_4$)~~ $\delta^{13}\mathrm{C(CH_4)}$ values have been offset (+1.4 ‰) to fit the ~~δ^{13}C(CH$_4$) global-mean~~ global mean $\delta^{13}\mathrm{C(CH_4)}$ in January 2012 and ~~CH$_4$ mixing ratios~~ CH_4 mole fractions have been scaled to fit the ~~CH$_4$ global-mean mixing ratios~~ global mean CH_4 mole fraction in January 2012. Due to the non-linearity of transport and mixing, offsetting ~~δ^{13}C(CH$_4$)~~ $\delta^{13}\mathrm{C(CH_4)}$ initial values in a forward run can generate errors. This impact is discussed later using a configuration where ~~δ^{13}C(CH$_4$)~~ $\delta^{13}\mathrm{C(CH_4)}$ initial conditions have not been offset (S1).

2.5 ~~Sensitivity tests~~

2.4.1 Sensitivity tests

~~Including REF, a set of 9 different configurations~~A set of nine different configurations, including REF, has been designed to assess the impact of assimilating ~~δ^{13}C(CH$_4$)~~ $\delta^{13}\mathrm{C(CH_4)}$ observations in addition to ~~CH$_4$~~ CH_4 observations and also to evaluate the sensitivity of the inversion results to the system's setup.

Multiple parameters have been tested throughout the various configurations :

1. NOISO has no isotopic ~~constraint~~constraint. Therefore, this configuration only simulates ~~CH$_4$ and assimilates CH$_4$ observations. δ^{13}C(CH$_4$) initial conditions in~~ CH_4 and assimilates CH_4 observations.
2. S1 uses $\delta^{13}\mathrm{C(CH_4)}$ initial conditions that are not offset and are therefore directly taken from the spin-up.
3. S2 assimilates the real ~~δ^{13}C(CH$_4$)~~ $\delta^{13}\mathrm{C(CH_4)}$ observations instead of the fitting curve data.
4. In S3, the ~~δ^{13}C(CH$_4$)~~ $\delta^{13}\mathrm{C(CH_4)}$ model uncertainties are divided by a factor 2.
5. T1 uses 10 sub-categories instead of 5 aggregated categories, increasing the degrees of freedom.

Table 2. Nomenclature and characteristics of the configurations. Details are provided in Sect.~~2.5~~ 2.4.1. ** Prior uncertainties ~~on~~ in initial ~~$\delta^{13}C(CH_4)$~~ $\delta^{13}C(CH_4)$ conditions have been set to 10 %.

Name	$\delta^{13}C(CH_4)$ initial cond.	$\delta^{13}C(CH_4)$ observations	$\delta^{13}C(CH_4)$ model errors	$\delta^{13}C(CH4)_{source}$ regional variability	$\delta^{13}C(CH4)_{source}$ uncertainties	Number of categories
NOISO	Without isotopic constraint					5
REF	Offset	Curve fitting	RMSE obs-fit	Regional variability	REF uncertainties	5
S1	No offset**	Curve fitting	RMSE obs-fit	Regional variability	REF uncertainties	5
S2	Offset	Real obs.	RMSE obs-fit	Regional variability	REF uncertainties	5
S3	Offset	Curve fitting	RMSE obs-fit / 2	Regional variability	REF uncertainties	5
T1	Offset	Curve fitting	RMSE obs-fit	Regional variability	REF uncertainties	10
T2	Offset	Curve fitting	RMSE obs-fit	Global mean	REF uncertainties	5
T3	Offset	Curve fitting	RMSE obs-fit	Regional variability	1 % for each cat.	5
T4	Offset	Curve fitting	RMSE obs-fit	Global mean	1 % for each cat.	5

6. In theory, the system is capable of optimally adjusting two source signatures if the assimilated information is sufficient. For instance, the system can choose to shift one signature downward and another upward in a given pixel, in order to improve the fitting in this specific pixel. The configuration T2 has been specifically designed to investigate whether the system would be able to retrieve a realistic distribution (similar to REF) starting from ~~globally averaged~~ globally-averaged signatures for each category.

7. In T3, the ~~$\delta^{13}C(CH_4)$~~ $\delta^{13}C(CH_4)$ source signatures uncertainties are set to a very low value (1 %) in order to prevent the system from optimizing them. In other words, all changes are put on ~~CH_4 emissions.~~ CH_4 emissions.

8. Finally, T4 applies both changes from T2 and T3. ~~Table 2~~

Table 2 summarizes the different configurations and the associated changes. The configurations have been grouped into two sets to facilitate the analysis of ~~the~~ results : on the one hand, S-group configurations (REF + S1-S4) have setup variations that are not expected to largely influence the results compared to REF. On the other hand, T-group configurations (T1-T4) alter parameters that are very likely to impact the results.

3 Results

3.1 Minimization of the cost function

The minimization process is performed using the M1QN3 algorithm (Gilbert and Lemaréchal, 1989). One full simulation (forward + adjoint) with the isotopic constraint necessitates about 170 CPU hours to run 6 years, i.e., 2.4 CPU hours per month simulated. The computational burden is increased by a factor 2 in comparison to an inversion without the isotopic constraint due to the doubling of simulated tracers (~~$^{12}CH_4$ and $^{13}CH_4$~~ $^{12}CH_4$ and $^{13}CH_4$). One full simulation is generally enough to complete one iteration of the minimization process but two or three simulations are sometimes required by M1QN3. Therefore, the number of simulations is slightly larger than the number of iterations. Figure~~3~~ 3 displays the minimization process of the cost function for all configurations.

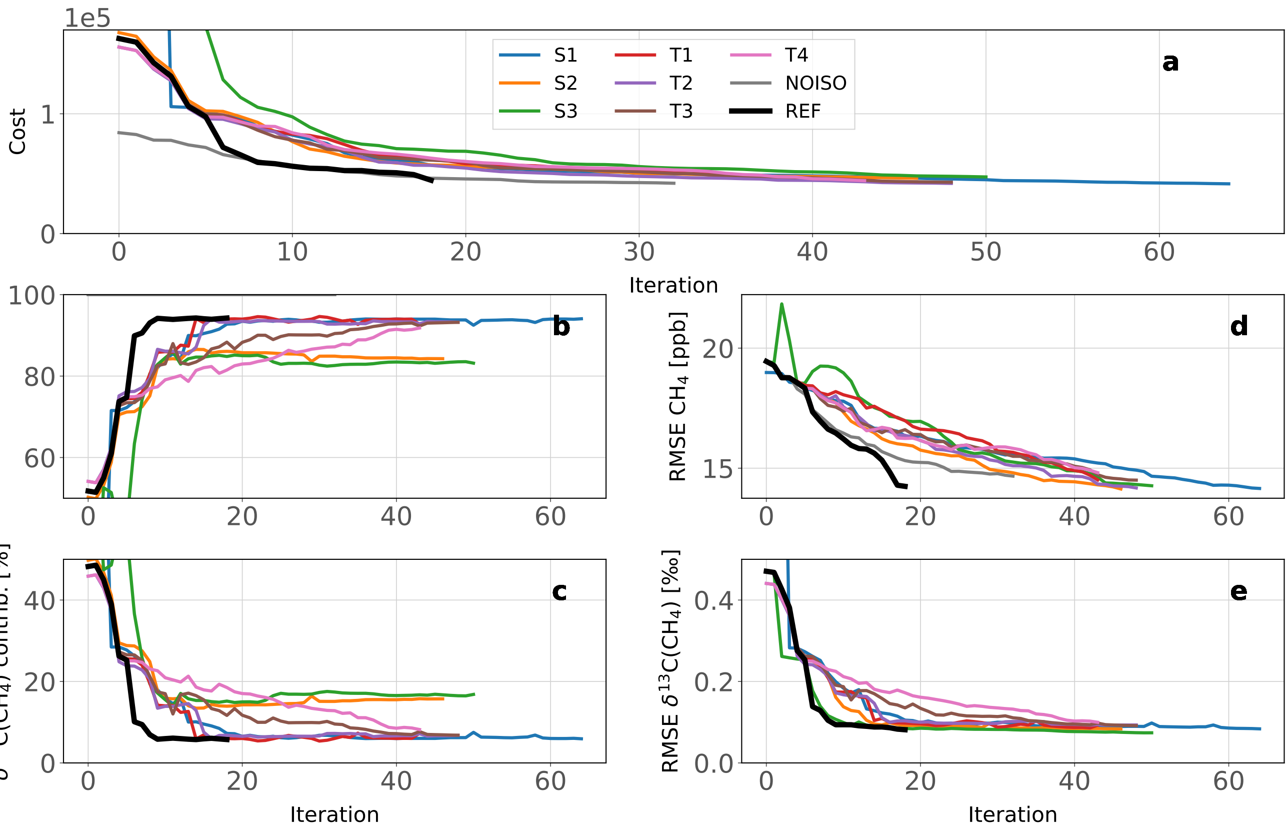

Figure 3. Minimization of the cost function for all configurations. a) ~~Cost~~ Value of the cost function with respect to the number of iterations. b) ~~CH_4~~ CH_4 contribution to J_o. c) ~~$\delta^{13}C(CH_4)$~~ $\delta^{13}C(CH_4)$ contribution to J_o. d) RMSE associated to observed-simulated ~~CH_4~~ CH_4. e) RMSE associated to observed-simulated ~~$\delta^{13}C(CH_4)$~~ $\delta^{13}C(CH_4)$. For clarity reasons, S1 and S3 initial values are not displayed because they are ~~too large compared to~~ much larger than those of REF.

Except for S1 and T1, the inversions were stopped when the gradient norm reduction exceeded 96 % for the third consecutive iteration. Number of iterations are compared to investigate the ~~sensibility~~ sensitivity of the computational cost to the setup. 32 iterations (37 simulations) for NOISO, 43 iterations (47 simulations) for REF and about 50 iterations for the others were necessary. Consequently, although assimilating ~~$\delta^{13}C(CH_4)$~~ $\delta^{13}C(CH_4)$ observations requires at least 11 additional iterations, the setup has little influence on the number of iterations if the same convergence criteria is used. Also, using curve-fitted data instead of real observations do not reduce the computational burden as we first speculated.

S1 and T1 inversions were extended until their cost function reached the same reduction as REF in order to estimate the additional computational burden required to reach similar results when initial conditions are not offset (S1) and the number of categories is increased (T1). 10 and 21 additional iterations were necessary for T1 and S1, respectively. For T1, it shows that increasing the degrees of freedom also increases the computational burden. For S1, it highlights the benefits of offsetting ~~$\delta^{13}C(CH_4)$~~ $\delta^{13}C(CH_4)$ initial conditions.

As we assume no correlation of errors in R, J_o (see Eq.~~3~~ 3) can be divided into ~~CH_4 and $\delta^{13}C(CH_4)$~~ CH_4 and $\delta^{13}C(CH_4)$ contributions. Figure 3 shows that all configurations lead to a fast reduction of the ~~$\delta^{13}C(CH_4)$~~ $\delta^{13}C(CH_4)$ contribution. During the first ten iterations, it decreased from 50-90 % (depending on the configuration) to 10-20 %. Conversely, the ~~CH_4~~ CH_4 contribution increased from 10-50 % to 80-90 %. By adjusting the ~~source isotopic~~ isotopic source signatures (all configurations besides T3-T4), the system was able to efficiently and rapidly reduce the discrepancies between simulated and observed ~~$\delta^{13}C(CH_4)$~~$\delta^{13}C(CH_4)$. As a result, the ~~$\delta^{13}C(CH_4)$~~ $\delta^{13}C(CH_4)$ RMSE decreased very rapidly during the first ten iterations while the ~~CH_4 RMSE due to CH_4 discrepancies~~ CH_4 RMSE decreased at a roughly constant rate. Consequently, the system is preferentially adjusting ~~$\delta^{13}C(CH_4)$ over CH_4~~ $\delta^{13}C(CH_4)$ over CH_4 values to reduce the cost function, presumably because the ratio of RMSE to prescribed observational error for $\delta^{13}C(CH_4)$ is, on average, about twice as large as for CH_4. In other terms, it is simpler for the system to adjust $\delta^{13}C(CH_4)$ before attempting to modify CH_4. The ratio of the number of $\delta^{13}C(CH_4)$ observations to the number of CH_4 observations is not expected to play a significant role in the convergence process, although we did not rigorously study this influence. This ratio is only expected to affect the contribution of a component ($\delta^{13}C(CH_4)$ or CH_4) to the total cost function.

The decrease rate associated with ~~$\delta^{13}C(CH_4)$~~ $\delta^{13}C(CH_4)$ RMSE can be increased by reducing the model uncertainties prescribed to the ~~$\delta^{13}C(CH_4)$~~ $\delta^{13}C(CH_4)$ observations. S3 is an example of such an adjustment, as the model uncertainties have been divided by two. With this configuration, the system requires five less iterations than REF to reach ~~similar $\delta^{13}C(CH_4)$~~ a similar $\delta^{13}C(CH_4)$ RMSE reduction but 7 additional iterations to reach ~~similar CH_4~~ a similar CH_4 RMSE reduction. T3 and T4 configurations ~~constrains~~ constrain the isotopic signatures, thus the reduction of the ~~$\delta^{13}C(CH_4)$~~ $\delta^{13}C(CH_4)$ contribution necessitates 25 more iterations than REF to reach similar RMSE reduction. To summarize, the decrease rate associated with ~~$\delta^{13}C(CH_4)$~~ $\delta^{13}C(CH_4)$ RMSE is highly dependent on the prescribed uncertainties in ~~$\delta^{13}C(CH_4)$~~ $\delta^{13}C(CH_4)$ observations and the ability of the system to adjust source signatures.

3.2 ~~CH_4~~ CH_4 and ~~$\delta^{13}C(CH_4)$~~ $\delta^{13}C(CH_4)$ fitting

As expected, the assimilation process greatly improves the agreement between simulated and observed values for both ~~CH_4 and $\delta^{13}C(CH_4)$~~CH_4 and $\delta^{13}C(CH_4)$. Figure 4 shows the globally-averaged time-series of ~~CH_4 and $\delta^{13}C(CH_4)$~~CH_4 and $\delta^{13}C(CH_4)$.

~~CH_4~~ CH_4 RMSE using prior estimates is 19.4 ppb and drops to 14.3 $\pm$ 0.2 ppb (1σ) on average over all the configurations using posterior estimates. Prior estimates ~~lead to simulated CH_4 mixing ratios in good agreement with observations~~ capture

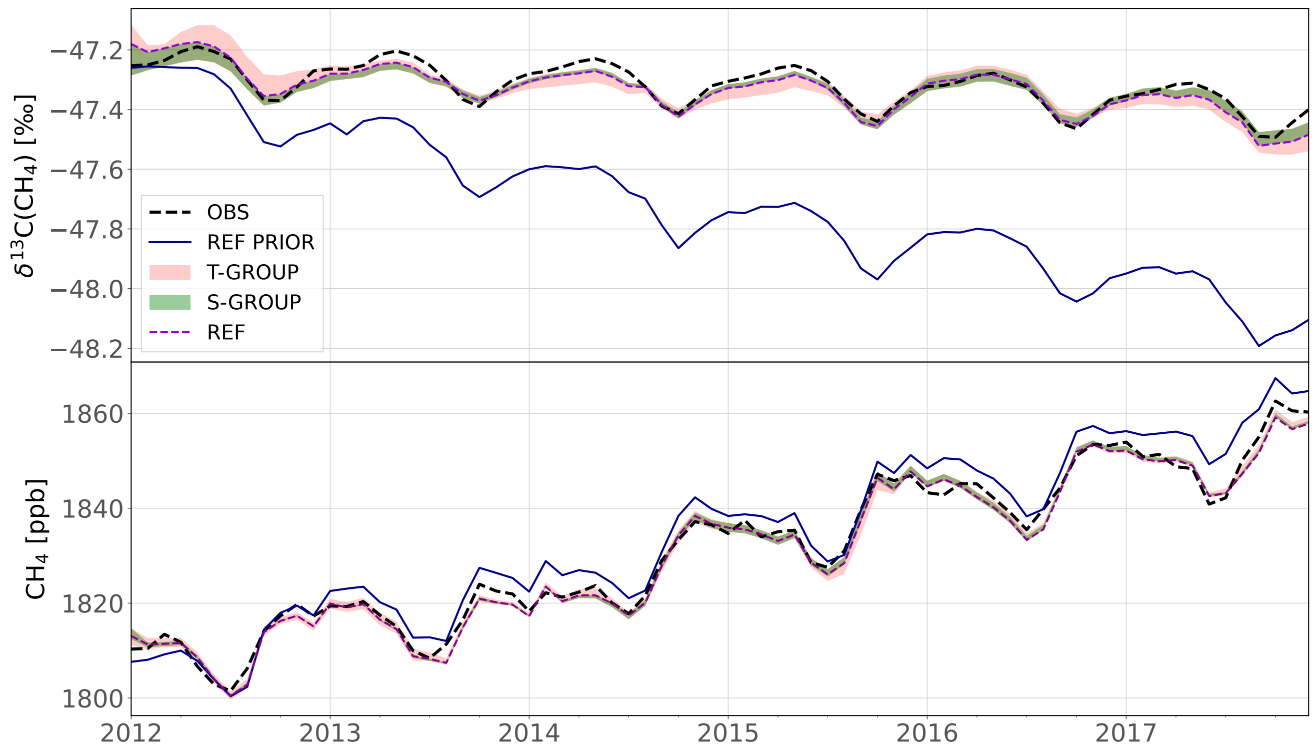

Figure 4. ~~Global-mean CH_4 mixing ratios~~ Global monthly $\delta^{13}C(CH_4)$ and ~~$\delta^{13}C(CH_4)$ values~~ CH_4 means between 2012 and 2017. The dashed black and solid blue lines in each panel denote the observed and ~~REF~~ prior ~~estimates~~simulated values (REF), respectively. The red and green ranges show the maximum and minimum values of the T-group and S-group, respectively. The thick and dashed ~~green~~ purple line denotes the posterior REF ~~configuration~~values. Globally-averaged values are computed using a method similar to Masarie and Tans (1995): a function including 3 polynomial parameters (quadratic) and 8 harmonic parameters is fitted to each time-series at available sites; the final value is obtained by performing a latitude-band weighted average over the Marine Boundary Layer (MBL) sites. The latitude band width was set at 30°. The posterior NOISO lines were not included because 1) the posterior NOISO global source signature is -54.1 ‰ and the line would therefore reach lower values than the REF PRIOR, affecting the visual clarity of the upper plot. 2) The posterior NOISO CH_4 values are extremely close to the REF values and including it would also affect the clarity of the lower plot.

well the observed CH_4 and the improvement is therefore relatively small. In addition, all configuration results regarding ~~CH_4~~ CH_4 are very similar. In particular, NOISO is not performing much differently than the other configurations, indicating that the additional isotopic constraint does not affect the fitting to ~~CH_4~~ CH_4 observations.

Prior ~~$\delta^{13}C(CH_4)$~~ $\delta^{13}C(CH_4)$ prescribed in REF are continuously decreasing from -47.2 to -48.2 ‰ and thus agrees very poorly (RMSE is 0.47 ‰) with observed values. This ~~is likely~~ can be due to an underestimation (too negative values) of some ~~source isotopic signatures~~ isotopic source signatures, an underestimation of the KIE values associated with the various sinks, an underestimation of the various sinks intensities (mostly Cl and OH) and/or a poor prior estimation of the source partitioning, i.e., an underestimation of ^{13}C-enriched sources (~~fossil fuels or biomass burning~~FF or BB) or an overestimation of ^{13}C-depleted sources (~~biogenic~~WET or AGW). The data assimilation process reconciles simulated and observed ~~$\delta^{13}C(CH_4)$~~ $\delta^{13}\mathrm{C}(\mathrm{CH}_4)$ (RMSE is 0.086 ± 0.008 ‰) for all configurations, albeit small differences depending on the setup emerge.

The S-group provides a better match to $\delta^{13}\mathrm{C}(\mathrm{CH}_4)$ observations than the T-group (0.081 ± 0.003 ‰ versus 0.091 ± 0.007 ‰). ~~Furthermore, the~~ The fit is very similar within the S-group. In contrast, the spread in the T-group is larger with ~~$\delta^{13}C(CH_4)$~~ $\delta^{13}\mathrm{C}(\mathrm{CH}_4)$ RMSE being equal to 0.093 ‰, 0.091 ‰ and 0.099 ‰ respectively for T2, T3 and T4. These results suggest that giving more freedom to the system to adjust the isotopic signatures and providing regional-specific estimates of prior source signatures instead of global values may be key elements for reaching better agreement. Best results (i.e., smallest RMSE) are obtained with T1 (0.079 ‰). However, this configuration necessitates 10 additional iterations to reach better results than REF. Without these additional iterations, REF would ~~be the best configuration~~ have the best results (0.081 ‰).

Figure 5 shows the RMSE distribution at all measurement sites for each configuration. All sites exhibit a RMSE reduction (from prior to posterior) for both ~~CH_4 and $\delta^{13}C(CH_4)$~~CH_4 and $\delta^{13}\mathrm{C}(\mathrm{CH}_4)$, except for BKT with T3 and T4 configurations. Furthermore, BKT, WKT, UUM, AMY and PON exhibit a posterior ~~CH_4~~ CH_4 RMSE above 25 ppb, showing that ~~CH_4~~ CH_4 measurements retrieved at these stations are not properly reproduced by the model, despite the optimization. ~~It can~~ Prescribed observation errors are likely not the main cause because mean values for these stations are large (10-15 ppb) but not the largest among all the assimilated stations. It can also be due to transport error or misrepresentation of sources close to the sites. Addressing this misfit is beyond the scope of this study, although the configuration influences the results : BKT and UUM fitting are notably deteriorated with T3 and T4 configurations. For example, BKT appears to be influenced by biomass burning sources in South-East Asia, which are strongly dependent on the configuration (see Sect.~~3.3~~ 3.3). Moreover, T3 provides the poorest ~~$\delta^{13}C(CH_4)$~~ $\delta^{13}\mathrm{C}(\mathrm{CH}_4)$ fitting at AMY (0.24 ‰). Therefore, ~~setting~~ using global values for source signatures and preventing the system from optimizing them lead to poorer fitting. On the contrary, T1 improves the results, indicating that additional degrees of freedom can help to reconcile simulations with observations, especially in South-East Asia and East Asia where these stations are located.

3.3 Global and regional emission increments

~~REF and NOISO emission increments for the period 2014-2015. Prior estimates (PRIOR) are identical for both configurations. The color-filled bars show the differences between REF posterior and prior estimates (REF increment). The hatched bars show the differences between NOISO posterior and prior estimates (NOISO increment). The upper panel refers to the global emissions. The lower panels refer to multiple regions of the globe. The regions are shown on the lower right panel. Red and blue error bars represent the minimum and maximum of the T-group and S-group, respectively. Circles on the red error bar show the results from the T-group.~~

We are primarily interested in the additional information provided by the assimilation of ~~$\delta^{13}C(CH_4)$~~ $\delta^{13}\mathrm{C}(\mathrm{CH}_4)$ data. Rather than discussing the regional and global ~~CH_4~~ CH_4 emissions and comparing these results to previous estimates, we investigate the differences between emissions inferred from configurations with and without the additional isotopic constraint. Long-term

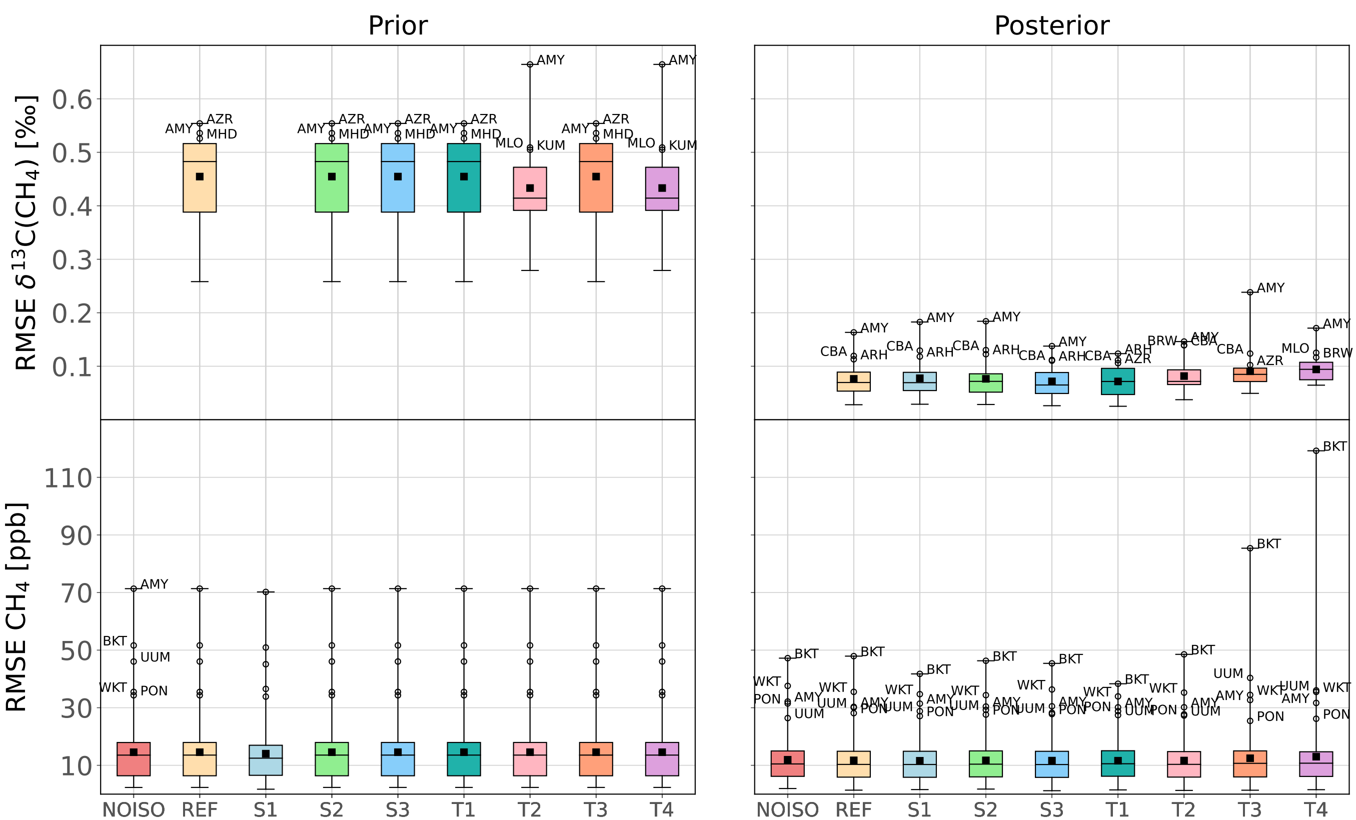

Figure 5. RMSE distribution ~~at~~ over the surface stations. Left panels show the prior ~~CH_4~~ CH_4 and ~~$\delta^{13}C(CH_4)$~~ $\delta^{13}C(CH_4)$ RMSE and right panels show the posterior RMSE. Upper panels show ~~$\delta^{13}C(CH_4)$~~ $\delta^{13}C(CH_4)$ RMSE and lower panels show ~~CH_4~~ CH_4 RMSE. For clarity reasons, S1 prior is not shown for ~~$\delta^{13}C(CH_4)$~~ $\delta^{13}C(CH_4)$ because the associated prior misfit is much larger than that of the other configurations. The box plot whiskers are covering the whole range of ~~the~~ data. In the lower-left panel, all station labels are identical, therefore most of them are removed to improve the clarity.

inversions will be run in the future with this system to provide more robust estimates of ~~CH_4~~ CH_4 emissions and compare them to the existing literature.

The inversion time-window is the ~~period~~ 2012-2017 period. However, flux and source signature ~~estimations of~~ estimates in the 2012-2013 and 2016-2017 periods are not interpreted as the system appears to require a 2-year spin-up (2012-2013) and a 2-year spin-down (2016-2017), over which the inversion problem is not sufficiently constrained and isotopic signatures vary widely over time. Therefore, only the 2014-2015 estimates are analyzed in Sect.~~3.3 and3.4~~ 3.3 and 3.4. Figure S2 in the supplement shows the time-series of isotopic signatures and illustrates this choice. These long effects are certainly caused by the relatively long relaxation timescales of isotopic ratios in the atmosphere (Tans, 1997) compared to that of total CH_4. Fully understanding this would require a lot of time and running multiple inversions (or possibly only tangent-linear simulations), starting from different initial conditions spanning the prescribed uncertainty envelope, to infer until when the initial atmospheric isotopic ratios and/or isotopic source signatures can influence the time-series of atmospheric isotopic ratios. This was too much work for this study but will certainly be addressed in future studies.

Figure 6 shows global and regional increments from the NOISO and REF inversions relative to prior estimates. Hereinafter, these differences will be referred to as "REF increment" (REF - PRIOR) and "NOISO increment" (NOISO - PRIOR). The difference between both increments will be called an "increment difference". Note that prior emissions are identical for all configurations. ~~At the global scale, the posterior total emission inferred with REF is 595.0~~ Posterior total emissions is 594.6 $\pm$ ~~1 and the difference between REF and NOISO is only 0.3~~ 1.2 $TgCH_4.yr^{-1}$ over all configurations, indicating that the isotopic constraint ~~does not affect the total~~ and setup configurations do not significantly affect posterior global emissions. A higher discrepancy between ~~these two~~ the budgets would have indicated a malfunction in the system as the ~~sinks are the same but this small value~~ prescribed sinks are identical. The small associated standard deviation is likely caused by a slight difference in the fitting to the observations and/or by the spatial variability of the prescribed sink coupled with ~~the~~ a small relocation of emissions depending on the configuration. For instance, OH concentrations are larger in the tropics and a relocation of emissions ~~when the isotopic constraint is implemented. Thus,~~ from the tropics to higher latitudes would be compensated for by larger global emissions. Between REF and NOISO, there is only a difference of 0.02 $TgCH_4.yr^{-1}$. We can therefore conclude that the additional isotopic constraint ~~only~~ either relocates the emissions ~~and also~~ or reallocates them between categories, as intended. All but one of the emission categories exhibit large changes between NOISO and REF : ~~wetlands (WT), fossil fuels (FF), microbial (MC) and biofuels-biomass burning (BB)~~ WET, FF, AGW and BB categories.

Overall, increments are large in regions with high emissions. Global increment differences ~~in MC (-6.4~~ (between REF and NOISO) in AGW (-6.4 $TgCH_4.yr^{-1}$) and FF emissions ($+8.6$ $TgCH_4.yr^{-1}$) are mainly due to regional increment ~~difference~~ differences in China and Temperate Asia. ~~MC regional increment difference is equal to -2.1~~ AGW regional increment differences are equal to -2.1 $TgCH_4.yr^{-1}$ in Temperate Asia and ~~-2.4~~ in China. Similarly, FF ~~increment difference is equal to~~ regional increment differences are equal to $+1.5$ $TgCH_4.yr^{-1}$ in Temperate Asia and $+5.0$ $TgCH_4.yr^{-1}$ in China. ~~WT~~ The WET global increment difference (~~-5.7~~ -5.7 $TgCH_4.yr^{-1}$) is mainly due to differences in Canada (~~-2.0~~ -2.0 $TgCH_4.yr^{-1}$) and South America (~~-2.3~~ -2.3 $TgCH_4.yr^{-1}$) but other regions such as Russia, Temperate Asia and South-East Asia are involved. BB emissions are also modified when implementing the isotopic constraint. Their global increment difference is

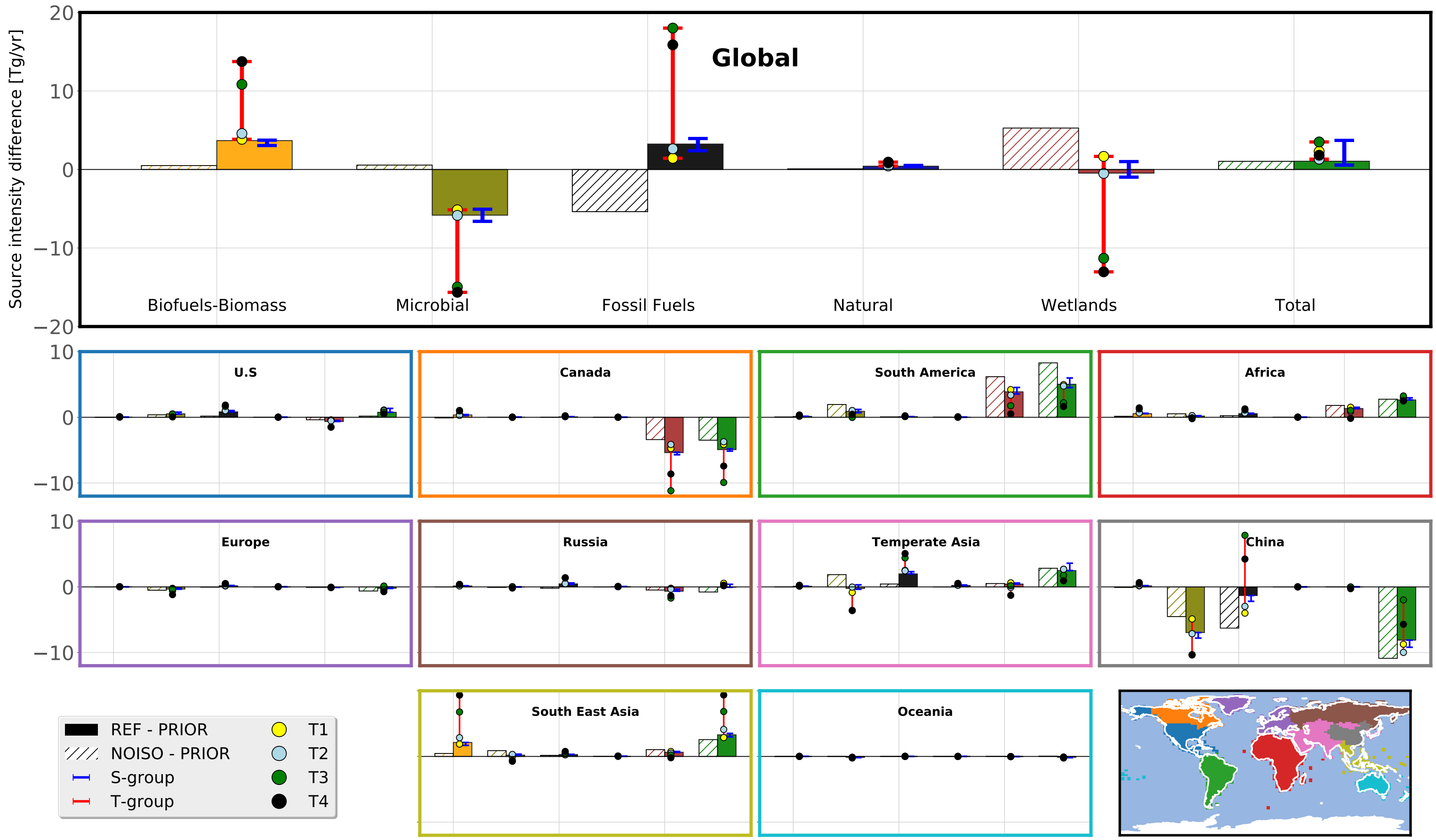

Figure 6. REF and NOISO emission increments for the 2014-2015 period. Prior estimates (PRIOR) are identical for both configurations. The color-filled bars show the differences between REF posterior and prior estimates (REF increment). The hatched bars show the differences between NOISO posterior and prior estimates (NOISO increment). The upper panel refers to the global emissions. The lower panels refer to multiple regions of the globe. The regions are shown on the lower right panel. Red and blue error bars represent the minimum and maximum of the T-group and S-group, respectively. Circles on the red error bar show the results from the T-group.

Table 3. Global ~~methane~~ CH_4 emissions by source category and region ($TgCH_4\,yr^{-1}$) for the REF configuration. Uncertainties are reported as the [min–max] range of all configurations.

	~~Biofuels-Biomass burning~~ BB	~~Microbial~~ AGW	~~Fossil Fuels~~ FF	~~Natural~~ NAT	~~Wetlands~~ WET	Total
U.S	1 [1 - 1]	22 [21 - 22]	14 [13 - 15]	2 [2 - 2]	17 [16 - 17]	56 [55 - 56]
Canada	2 [1 - 3]	2 [2 - 2]	2 [2 - 2]	1 [1 - 1]	21 [16 - 23]	29 [24 - 30]
South America	2 [2 - 3]	30 [29 - 31]	6 [6 - 6]	5 [5 - 5]	53 [50 - 55]	96 [93 - 99]
Africa	9 [8 - 10]	25 [25 - 26]	14 [13 - 15]	4 [4 - 4]	28 [26 - 28]	80 [80 - 80]
Europe	1 [1 - 1]	20 [19 - 20]	6 [6 - 7]	2 [2 - 2]	4 [4 - 4]	34 [33 - 34]
Russia	2 [2 - 2]	5 [5 - 5]	12 [12 - 13]	3 [3 - 3]	12 [11 - 13]	35 [34 - 36]
Temperate Asia	3 [3 - 3]	54 [51 - 56]	28 [27 - 31]	7 [7 - 7]	13 [11 - 13]	105 [104 - 106]
China	5 [5 - 5]	29 [26 - 32]	24 [19 - 33]	1 [1 - 1]	5 [5 - 5]	64 [61 - 70]
South East Asia	11 [9 - 18]	23 [22 - 23]	8 [7 - 8]	4 [3 - 4]	22 [21 - 23]	66 [66 - 72]
Oceania	1 [0 - 1]	4 [4 - 5]	2 [2 - 2]	1 [1 - 1]	3 [3 - 3]	11 [11 - 11]
Others	1 [1 - 1]	4 [4 - 4]	5 [5 - 5]	8 [8 - 8]	2 [2 - 2]	19 [19 - 19]
Global	37 [33 - 47]	220 [210 - 226]	119 [111 - 134]	38 [38 - 39]	180 [167 - 185]	594 [594 - 597]

equal to +3.2 $TgCH_4.yr^{-1}$ principally owing to regional increment differences in South-East Asia (+1.7 $TgCH_4.yr^{-1}$), Canada (+0.4 $TgCH_4.yr^{-1}$) and Africa (+0.4 $TgCH_4.yr^{-1}$). The ~~Natural (NAT)~~ NAT category exhibit very little changes (less than 1 $TgCH_4.yr^{-1}$), even in relative values~~(see Fig. S3 in the supplement)~~.

S-group configurations infer ~~results remaining~~ posterior results that are consistent with REF, with only small variations depending on the category and the region (see Table S5 in the supplement). In particular, S1 provides roughly the same results as REF but with more iterations, highlighting again that offsetting the initial conditions can help to reduce the computational burden without affecting the results. On the contrary, T-group configurations are affecting the increments, although T1 and T2 configurations are generally much closer to REF than T3 and T4. T1 (yellow dot) and T2 (blue dot) ~~exhibits~~ exhibit differences with the S-group ~~essentially~~ mainly in China where ~~WT~~ WET and FF increments are modified ($\sim$ ~~-3~~ -3 $TgCH_4.yr^{-1}$). More importantly, almost freezing the isotopic signatures to their prior values ~~in this system~~ (T3 and T4) results in increment differences 3 to 4 times larger than with REF, i.e., more than 10 $TgCH_4.yr^{-1}$ at the global scale. It highlights the dependence of the inferred ~~CH_4~~ CH_4 emissions to the prior source signatures estimates. In other words, the quality of isotopic ~~signature~~ source signatures (values and ~~distributions~~uncertainties) appears to be critical for the robustness of ~~the system's source estimates.~~ emissions estimates.

3.4 Global and regional source signature increments

~~Source isotopic~~ Isotopic source signatures are also optimized by the system. Figure 7 provides the differences of flux-weighted source ~~isotopic signatures for different regions. It shows the difference~~ signatures between REF posterior and prior estimates for different regions and each emission category.

~~All source signature~~ With configurations that allow the source signatures to be optimized, all source signatures are shifted upwards by the inversions ~~,~~ in order to correct the ~~too~~ excessively strong negative trend in ~~$\delta^{13}C(CH_4)$~~ $\delta^{13}C(CH_4)$. At the

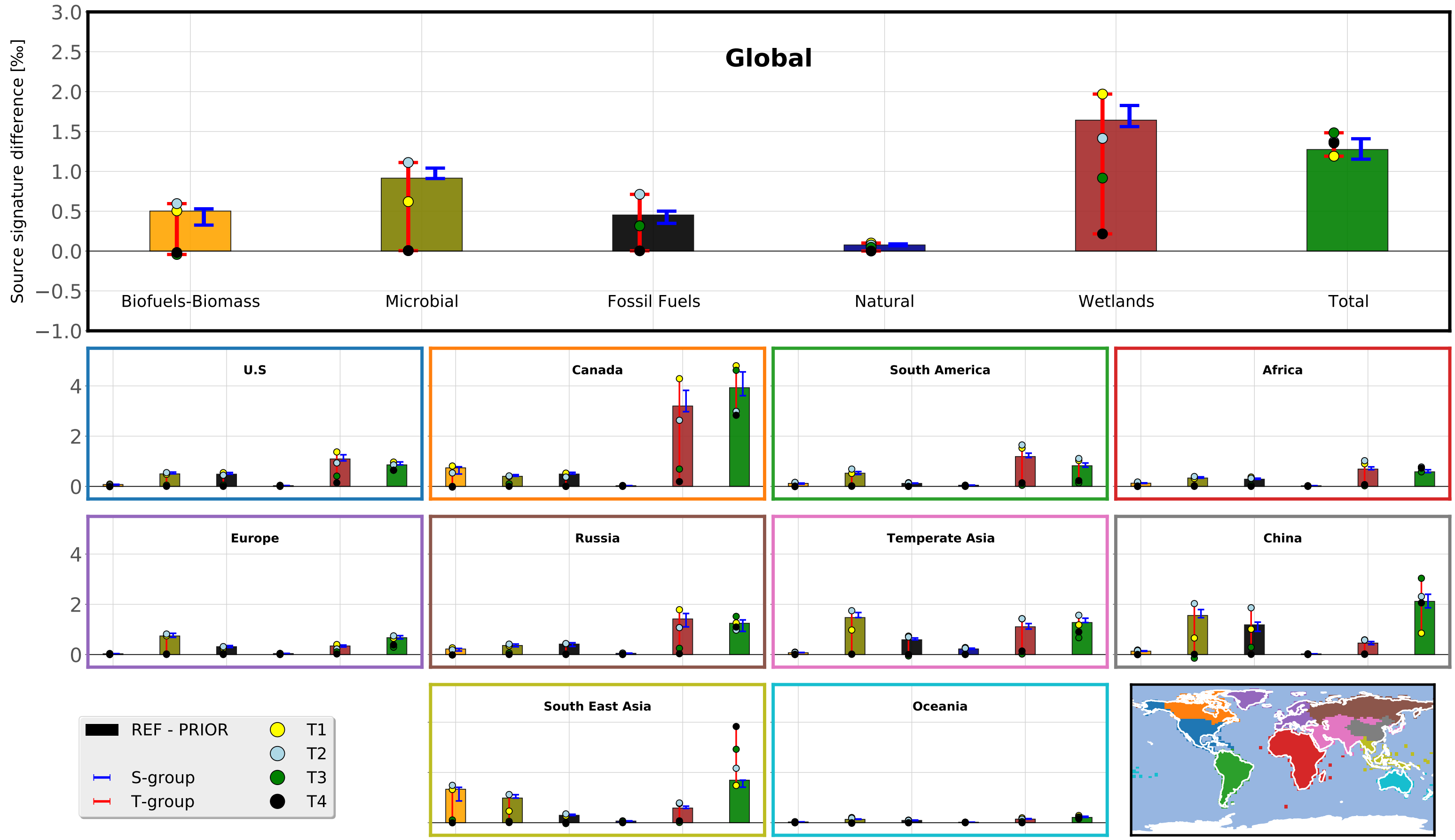

Figure 7. REF flux-weighted source signature increments for the ~~period~~ 2014-2015 ~~. Posterior fluxes are used to compute flux-weighted averages~~period. The color-filled bars show the differences between REF posterior and prior estimates (REF increment). The upper panel refers to the global emissions. The lower panels refer to multiple regions of the globe. The regions are shown on the lower right panel. Red and blue error bars represent the minimum and maximum of the T-group and S-group, respectively. Circles on error bars show the results from the T-group.

global scale, the flux-weighted source signatures of ~~WT~~WET, FF, ~~MC and BB~~ AGW, BB and NAT are increased by 1.7, 0.5, 0.9~~and~~ , 0.5 and 0.1 ‰, respectively. The global source signature is increased from ~~-53.9~~ −53.9 ‰ (prior) to ~~-52.6~~ −52.6 ± 0.2 ‰ (posterior ~~) depending on the configuration (see~~ with standard deviation over the configurations). More information is provided in the supplement (Table S6). The posterior global signature is strongly dependent on the ~~total fractionation effect~~KIE of atmospheric oxidation. This effect tends to deplete air in ~~$^{13}CH_4$~~$^{13}CH_4$, shifting the ~~$\delta^{13}C(CH_4)$~~ $\delta^{13}C(CH_4)$ to more positive values as the ~~CH_4~~ CH_4 molecules emitted by the sources are removed from the atmosphere. The ~~total fractionation effect~~ mean KIE in our simulations depends on 1) the prescribed OH, O(^{1}D) and Cl concentrations and 2) the prescribed KIE values associated to the ~~sinks (see Text S2 in the supplement)~~individual sinks. As the ~~fractionation effect~~ mean KIE is the same for all configurations, the posterior global source signatures are very close.

The ~~WT source signature~~WET global source signature, associated with REF posterior estimates, exhibits the larger upward shift compared to prior estimates, from a ~~global value of -60.8~~ value of −60.8 ‰ to ~~-59.1~~ −59.1 ‰. ~~This large difference for an average signature is due to upward shifts in Boreal~~ Large upward WET source signature shifts are located in boreal regions (North America, Russia) but also in South America and Temperate Asia. The ~~MC~~ AGW source signature is increased by 0.9 ‰ mainly due to changes in Asia. The FF source signature is increased by 0.5 ‰ ~~globally~~ due to a large increment in China (~~+~~ +1.2 ‰). Finally, the BB source signature is ~~reevaluated~~ modified in South-East Asia (~~+~~ +1.4 ‰) and Canada (~~+~~ +0.8 ‰).

These changes are consistent within the S-group (see blue errorbars in Fig.~~7~~ 7), although small variations are visible (e.g., ± 0.3 ‰ for ~~WT~~ WET in Canada). The source signature is therefore modified nearly to the same extent in all regions, no matter which configuration in the S-group is analyzed. ~~More details on prior and posterior values are given in the supplement (Table S6).~~ T1 (see yellow dot in Fig.~~7~~ 7), with more optimized categories than the others, shows small differences at the global scale (less than 0.3 ‰ for all categories), although differences of more than 1 ‰ are ~~visible~~ found in China. Therefore, increasing the number of degrees of freedom lead to similar flux estimates but can affect the signatures at regional scale.

T2 estimates are shifted upward to reach a less negative global ~~source isotopic~~ isotopic source signature without getting closer to the regional distribution of the S-group. This is likely caused by the scarcity of ~~$\delta^{13}C(CH_4)$~~ $\delta^{13}C(CH_4)$ stations and correcting this behavior seems challenging without additional observations. The problem might be circumvented by using the region scale rather than the pixel scale to optimize isotopic signature values. Future inversions will test this assumption.

3.5 Posterior uncertainties

Formally, posterior uncertainties are given by the Hessian of the cost function. This matrix can hardly be computed at an achievable cost considering the size of the inverse problem. Other means must be implemented to get posterior ~~uncertainties~~ uncertainty such as estimating lower-rank approximation of the Hessian, using Monte-Carlo ensembles of variational inversion to represent the prior uncertainties or computing multiple configurations covering a given range of possibilities. Here, using multiple configurations ~~provide~~ provides insight into the posterior uncertainty ~~(min-max range)~~ associated with the posterior fluxes. ~~WT, MC~~We calculated the full uncertainty range using the minimum and maximum values among all the configurations, as in Saunois et al. (2020). WET, AGW, FF and BB flux estimates (Table~~3~~ 3) exhibit an uncertainty of 10 %, 7 %, 19 % and 38 %, respectively. BB is the most uncertain estimate ~~relatively~~ relative to its intensity, although FF ~~show~~

shows the largest absolute uncertainty (23~~).~~ $\mathrm{TgCH_4.yr^{-1}}$). These uncertainties are unlikely to be affected by the assimilation of additional $\delta^{13}\mathrm{C(CH_4)}$ data because we expect the uncertainties on the isotopic source signatures to have a much larger influence. However, this remains to be tested in future work if posterior uncertainties can be calculated.

At present, M1QN3 is not the only optimization algorithm that can be utilized to perform variational inversions in the CIF. The CONGRAD algorithm (Fisher, 1998), that follows a conjugate gradient method combined with a Lanczos algorithm, is also implemented. In particular, it considerably facilitates the computation of posterior uncertainties. Any change in algorithm is very easy and accessible to any CTM embedded in the CIF. However, CONGRAD has not been tested yet with $\delta^{13}\mathrm{C(CH_4)}$ data. As CONGRAD is only designed for linear problems, using this algorithm could radically change the results of inversions performed with the isotopic constraints and future work will focus on using CONGRAD to perform the inversions with isotopic constraints.

4 Conclusions and perspectives

We present here a new variational inversion system designed to assimilate observations of both a specific trace gas and its isotopic data. This system allows to optimize both ~~the~~ tracer emissions and ~~the~~ associated isotopic signatures for multiple source categories. To test this system we have assimilated ~~CH_4 and $\delta^{13}C(CH_4)$~~ $\mathrm{CH_4}$ and $\delta^{13}\mathrm{C(CH_4)}$ data retrieved at different measurement sites over the globe.

Different configurations have been tested in order to assess the ~~sensibility~~ sensitivity of the system to the setup. We have shown that offsetting the ~~$\delta^{13}C(CH_4)$~~ $\delta^{13}\mathrm{C(CH_4)}$ initial conditions before the inversion (S1), using ~~$\delta^{13}C(CH_4)$~~ $\delta^{13}\mathrm{C(CH_4)}$ curve fitting data instead of the original observations (S2) and reducing the prescribed uncertainties in the ~~$\delta^{13}C(CH_4)$~~ $\delta^{13}\mathrm{C(CH_4)}$ observations (S3) have very little effect on the inferred fluxes (less than 2 $\mathrm{TgCH_4.yr^{-1}}$ for each category at the global scale). However, offsetting ~~the $\delta^{13}C(CH_4)$~~ $\delta^{13}\mathrm{C(CH_4)}$ initial conditions before the inversion results in a reduced computational time (21 less iterations).

Other setup choices have more influence on the results. Increasing the number of source categories (T1) requires more computational time (10 more iterations) to reach a cost function (and RMSE) reduction similar to REF. Moreover, although the global posterior emissions with an increased number of categories are very close to those inferred with REF (less than 1 $\mathrm{TgCH_4.yr^{-1}}$), the posterior isotopic signatures can be modified in some regions (more than 1 ‰ in China). Also, starting from ~~mean global~~ globally-averaged values for the source signatures (T2) makes the system unable to retrieve the regional-specific isotopic signatures from REF. Increasing the number of ~~$\delta^{13}C(CH_4)$~~ $\delta^{13}\mathrm{C(CH_4)}$ observations could help to cope with this issue. Finally, configurations ~~which constrain~~ constraining the source signatures (T3-T4) show differences in global flux estimates of more than 10 $\mathrm{TgCH_4.yr^{-1}}$, compared to REF. This emphasizes the need for good prior source signature estimates.

The major ~~caveat~~ drawback of this inversion system is undoubtedly the large computational burden of a full minimization process. At least 40 iterations appear to be necessary to reach a satisfying convergence state at the regional scale. For the LMDz-SACS model, a maximum of 8 CPUs can be run in parallel, resulting in an elapsed time of 5-6 weeks to run one of the inversions of this study. A new generation of transport models such as DYNAMICO (Dubos et al., 2015) could help to address this problem in the future by allowing more processors to run in parallel. Also, further developments will implement some parallelization methods to enable computational burden reduction (e.g., Chevallier, 2013). In addition, variational inversions as implemented in the CIF ~~are not enabled to~~ do not provide a quantification (even approximated) of the posterior uncertainties. Dedicated efforts need to be done to address this issue in the future, at an achievable numerical cost. In particular, using the CONGRAD algorithm instead of M1QN3 could be a solution as both algorithms can be easily selected in the CIF. However, additional work is needed to ensure that switching the optimization algorithm does not affect the results inferred with our new system.

This system is implemented within the CIF framework and can therefore be used for inversions with the various CTMs embedded in the CIF, provided the adjoint codes of the models exist. ~~Due~~ As the operations developed for the purpose of this study are performed outside the model structure, forward, tangent-linear and adjoint codes from other CTMs do not require any modifications as long as the model is capable of simulating both $^{12}CH_4$ and $^{13}CH_4$ simultaneously. The prior input must be adapted to the new model (spatial and time resolution) but the format of the observational data and of the prescribed errors can be preserved. Also, due to the variational method benefits, the efforts dedicated to the preparation of inputs do not scale with either the size of the observational datasets or the length of the simulation time-window. Therefore, this system is very powerful and is particularly relevant to study in a consistent way the influence of multiple physical parameters on atmospheric isotopic ratios, such as the transport, the isotopic signatures, the emission scenarios, the KIE values, etc. We did not try to assess here the sensitivity of the system to these parameters as only technical aspects of the system were tested. This will be part of ~~a future analysis~~future analyses.

~~$\delta^{13}C(CH_4)$~~ As mentioned in the introduction, future work will address the estimation of CH_4 emissions over longer periods of time using this new system. For instance, the 2000-2006 CH_4 stabilization period and the subsequent renewed growth are particularly interesting to study using the isotopic constraint as global $\delta^{13}C(CH_4)$ started to decrease after 2006. These periods of time have already attracted considerable critical attention from many inversion studies (with or without the isotopic constraint) and comparing the results derived from such a complete 3-D variational inversion system with other recent estimates should be highly relevant. The most important limitation of assimilating $\delta^{13}C(CH_4)$ lies in the fact that very limited $\delta^{13}C(CH_4)$ data are available, and therefore evaluating the posterior simulated $\delta^{13}C(CH_4)$ is often challenging, if not impossible. However, satellite and balloon / AirCore data can easily be used to evaluate the posterior simulated CH_4.

$\delta^{13}C(CH_4)$ is not the only isotopic data that can be assimilated in such a system. Many δD(~~CH_4~~CH_4) observations have also been retrieved during the ~~period~~ 2004-2010 period at many different locations. These isotopic values can provide additional information that can further help to discriminate the co-emitted ~~CH_4~~ CH_4 fluxes (Rigby et al., 2012). Moreover, ethane (C_2H_6) is co-emitted with ~~CH_4~~ CH_4 by fossil fuel extraction and distribution (Kort et al., 2016; Smith et al., 2015) and observations are available at a multitude of sites since the early 1980s. Therefore, assimilating this data can provide additional constraint. The system will therefore be improved in the future in order to assimilate ~~$\delta^{13}C(CH_4)$~~$\delta^{13}C(CH_4)$, δD(~~CH_4~~CH_4) and C_2H_6 observations together.

Data availability. The code files of the CIF version used in the present paper are registered under the following link : https://doi.org/10.5281/zenodo.6304912. Prior anthropogenic fluxes (EDGARv4.3.2) can be downloaded from the EDGAR website (https://edgar.jrc.ec.europa.eu/dataset_ghg432). Biomass burning fluxes can be downloaded from the GFED website (https://globalfiredata.org/pages/data/). Prior natural fluxes and other data are available upon request (joel.thanwerdas@lsce.ipsl.fr). The CH_4 data used in the present paper were provided by many stations and measurement networks around the world (a comprehensive list can be found in the supplement and in the acknowledgments). Their data is freely available upon request to the station maintainers or via dedicated websites. The $\delta^{13}C(CH_4)$ observational data can be downloaded from the NOAA-GML website (https://gml.noaa.gov/dv/data/).

Author contributions. JT implemented the variational inversion system within the CIF with the precious help of AB. JT designed, run and analyzed the tested configurations. AB, MS, IP and PB provided scientific and technical expertise. They also contributed to the analysis of this work. BV and SEM provided the $\delta^{13}C(CH_4)$ data and scientific expertise regarding $\delta^{13}C(CH_4)$ observations. JT prepared the manuscript with contributions from all co-authors.

Competing interests. The authors declare that they have no conflict of interest.

Acknowledgements. This work was supported by the CEA (Commissariat à l'Energie Atomique et aux Energies Alternatives). The study extensively relies on the meteorological data provided by the ECMWF. Calculations were performed using the computing resources of LSCE, maintained by François Marabelle and the LSCE IT team. ~~We are~~ The authors thank the reviewers (Peter Rayner and two anonymous referees) for their fruitful comments and suggestions on our manuscript. We are also grateful to many station maintainers that provided the CH_4 data: **For AGAGE network** - AGAGE is supported principally by NASA (USA) grants to MIT and SIO, and also by: BEIS (UK) and NOAA (USA) grants to Bristol University; CSIRO and BoM (Australia): FOEN grants to Empa (Switzerland); NILU (Norway); SNU (Korea); CMA (China); NIES (Japan); and Urbino University (Italy); **For South African Weather Service Cape Point GAW station** - We thank Casper Labuschagne, Thumeka Mkololo and Warren Joubert ; **For EC network** - We thank Doug Worthy; **For MGO network** - We thank Nina Paramonova and Victor Ivakhov; **For AMY network** - We thank Haeyoung Lee and Sepyo Lee - The AMY data was funded by the Korea Meteorological Administration Research and Development Program under grant KMA2018-00522; **For ENEA network** - We thank Alcide Disarra, Salvatore Piacentino and Damiano Sferlazzo; **For EMPA network** - We thank Martin Steinbacher and Brigitte Buchmann - The CH_4 measurements at JFJ are run by EMPA in collaboration with FOEN and are also supported by ICOS-CH; **For BMKG-EMPA network** - We thank Martin Steinbacher, Alberth Christian and Sugeng Nugroho - The CH_4 measurements at BKT are run by BMKG in collaboration with EMPA;

References

Berchet, A., Sollum, E., Thompson, R. L., Pison, I., Thanwerdas, J., Broquet, G., Chevallier, F., Aalto, T., Bergamaschi, P., Brunner, D., Engelen, R., Fortems-Cheiney, A., Gerbig, C., Groot Zwaaftink, C., Haussaire, J.-M., Henne, S., Houweling, S., Karstens, U., Kutsch, W. L., Luijkx, I. T., Monteil, G., Palmer, P. I., van Peet, J. C. A., Peters, W., Peylin, P., Potier, E., Rödenbeck, C., Saunois, M., Scholze, M., Tsuruta, A., and Zhao, Y.: The Community Inversion Framework v1.0: a unified system for atmospheric inversion studies, Geoscientific Model Development Discussions, pp. 1–41, https://doi.org/https://doi.org/10.5194/gmd-2020-407, 2020.

Berchet, A., Sollum, E., Thompson, R. L., Pison, I., Thanwerdas, J., Broquet, G., Chevallier, F., Aalto, T., Berchet, A., Bergamaschi, P., Brunner, D., Engelen, R., Fortems-Cheiney, A., Gerbig, C., Groot Zwaaftink, C. D., Haussaire, J.-M., Henne, S., Houweling, S., Karstens, U., Kutsch, W. L., Luijkx, I. T., Monteil, G., Palmer, P. I., van Peet, J. C. A., Peters, W., Peylin, P., Potier, E., Rödenbeck, C., Saunois, M., Scholze, M., Tsuruta, A., and Zhao, Y.: The Community Inversion Framework v1.0: a unified system for atmospheric inversion studies, Geoscientific Model Development, 14, 5331–5354, https://doi.org/10.5194/gmd-14-5331-2021, 2021.

Bergamaschi, P., Lubina, C., Königstedt, R., Fischer, H., Veltkamp, A. C., and Zwaagstra, O.: Stable isotopic signatures (δ^{13}C, δD) of methane from European landfill sites, Journal of Geophysical Research: Atmospheres, 103, 8251–8265, https://doi.org/10.1029/98JD00105, 1998.

Bergamaschi, P., Krol, M., Meirink, J. F., Dentener, F., Segers, A., Aardenne, J. v., Monni, S., Vermeulen, A. T., Schmidt, M., Ramonet, M., Yver, C., Meinhardt, F., Nisbet, E. G., Fisher, R. E., O'Doherty, S., and Dlugokencky, E. J.: Inverse modeling of European CH_4 emissions 2001–2006, Journal of Geophysical Research: Atmospheres, 115, https://doi.org/https://doi.org/10.1029/2010JD014180, 2010.

Bergamaschi, P., Houweling, S., Segers, A., Krol, M., Frankenberg, C., Scheepmaker, R. A., Dlugokencky, E., Wofsy, S. C., Kort, E. A., Sweeney, C., Schuck, T., Brenninkmeijer, C., Chen, H., Beck, V., and Gerbig, C.: Atmospheric CH_4 in the first decade of the 21st century: Inverse modeling analysis using SCIAMACHY satellite retrievals and NOAA surface measurements, Journal of Geophysical Research: Atmospheres, 118, 7350–7369, https://doi.org/10.1002/jgrd.50480, 2013.

Bergamaschi, P., Karstens, U., Manning, A. J., Saunois, M., Tsuruta, A., Berchet, A., Vermeulen, A. T., Arnold, T., Janssens-Maenhout, G., Hammer, S., Levin, I., Schmidt, M., Ramonet, M., Lopez, M., Lavric, J., Aalto, T., Chen, H., Feist, D. G., Gerbig, C., Haszpra, L., Hermansen, O., Manca, G., Moncrieff, J., Meinhardt, F., Necki, J., Galkowski, M., O'Doherty, S., Paramonova, N., Scheeren, H. A., Steinbacher, M., and Dlugokencky, E.: Inverse modelling of European $\mathrm{CH_4}$ emissions during 2006–2012 using different inverse models and reassessed atmospheric observations, Atmospheric Chemistry and Physics, 18, 901–920, https://doi.org/https://doi.org/10.5194/acp-18-901-2018, 2018.

Bousquet, P., Ciais, P., Miller, J. B., Dlugokencky, E. J., Hauglustaine, D. A., Prigent, C., Van der Werf, G. R., Peylin, P., Brunke, E.-G., Carouge, C., Langenfelds, R. L., Lathière, J., Papa, F., Ramonet, M., Schmidt, M., Steele, L. P., Tyler, S. C., and White, J.: Contribution of anthropogenic and natural sources to atmospheric methane variability, Nature, 443, 439–443, https://doi.org/10.1038/nature05132, 2006.

Bréas, O., Guillou, C., Reniero, F., and Wada, E.: The Global Methane Cycle: Isotopes and Mixing Ratios, Sources and Sinks, Isotopes in Environmental and Health Studies, 37, 257–379, https://doi.org/10.1080/10256010108033302, 2001.

Chang, J., Peng, S., Ciais, P., Saunois, M., Dangal, S. R. S., Herrero, M., Havlík, P., Tian, H., and Bousquet, P.: Revisiting enteric methane emissions from domestic ruminants and their $\delta^{13}\mathrm{CCH_4}$ source signature, Nature Communications, 10, 3420, https://doi.org/10.1038/s41467-019-11066-3, 2019.

Chanton, J. P., Rutkowski, C. M., and Mosher, B.: Quantifying Methane Oxidation from Landfills Using Stable Isotope Analysis of Downwind Plumes, Environmental Science & Technology, 33, 3755–3760, https://doi.org/10.1021/es9904033, 1999.

Chanton, J. P., Rutkowski, C. M., Schwartz, C. C., Ward, D. E., and Boring, L.: Factors influencing the stable carbon isotopic signature of methane from combustion and biomass burning, Journal of Geophysical Research: Atmospheres, 105, 1867–1877, https://doi.org/10.1029/1999JD900909, 2000.

Chevallier, F.: On the parallelization of atmospheric inversions of CO2 surface fluxes within a variational framework, Geoscientific Model Development, 6, 783–790, https://doi.org/doi.org/10.5194/gmd-6-783-2013, 2013.

Chevallier, F., Fisher, M., Peylin, P., Serrar, S., Bousquet, P., Bréon, F.-M., Chédin, A., and Ciais, P.: Inferring CO_2 sources and sinks from satellite observations: Method and application to TOVS data, Journal of Geophysical Research, 110, https://doi.org/10.1029/2005JD006390, 2005.

Craig, H.: Isotopic standards for carbon and oxygen and correction factors for mass-spectrometric analysis of carbon dioxide, Geochimica et Cosmochimica Acta, 12, 133–149, https://doi.org/10.1016/0016-7037(57)90024-8, 1957.

Dlugokencky, E.: NOAA/GML, www.esrl.noaa.gov/gmd/ccgg/trends_ch4/, 2021.

Dubos, T., Dubey, S., Tort, M., Mittal, R., Meurdesoif, Y., and Hourdin, F.: DYNAMICO-1.0, an icosahedral hydrostatic dynamical core designed for consistency and versatility, Geoscientific Model Development, 8, 3131–3150, https://doi.org/10.5194/gmd-8-3131-2015, 2015.

Enting, I. G. and Newsam, G. N.: Atmospheric constituent inversion problems: Implications for baseline monitoring, Journal of Atmospheric Chemistry, 11, 69–87, https://doi.org/10.1007/BF00053668, 1990.

Etiope, G.: Natural Gas Seepage: The Earth's Hydrocarbon Degassing, Springer International Publishing, https://www.springer.com/gp/book/9783319146003, 2015.

Etminan, M., Myhre, G., Highwood, E. J., and Shine, K. P.: Radiative forcing of carbon dioxide, methane, and nitrous oxide: A significant revision of the methane radiative forcing, Geophysical Research Letters, 43, 12,614–12,623, https://doi.org/https://doi.org/10.1002/2016GL071930, 2016.

Fisher, M.: Minimization algorithms for variational data assimilation, www.ecmwf.int/en/elibrary/9400-minimization-algorithms-variational-data-assimilation, (last access: 23 August 2021), 1998.

Fletcher, S. E. M., Tans, P. P., Bruhwiler, L. M., Miller, J. B., and Heimann, M.: CH_4 sources estimated from atmospheric observations of CH_4 and its $^{13}C/^{12}C$ isotopic ratios: 2. Inverse modeling of CH_4 fluxes from geographical regions, Global Biogeochemical Cycles, 18, https://doi.org/10.1029/2004GB002224, 2004.

Fujita, R., Morimoto, S., Maksyutov, S., Kim, H.-S., Arshinov, M., Brailsford, G., Aoki, S., and Nakazawa, T.: Global and Regional CH_4 Emissions for 1995–2013 Derived From Atmospheric CH_4, $\delta^{13}C$-CH_4, and δD-CH_4 Observations and a Chemical Transport Model, Journal of Geophysical Research: Atmospheres, 125, e2020JD032 903, https://doi.org/https://doi.org/10.1029/2020JD032903, 2020.

Ganesan, A. L., Stell, A. C., Gedney, N., Comyn-Platt, E., Hayman, G., Rigby, M., Poulter, B., and Hornibrook, E. R. C.: Spatially Resolved Isotopic Source Signatures of Wetland Methane Emissions, Geophysical Research Letters, 45, 3737–3745, https://doi.org/10.1002/2018GL077536, 2018.

Gilbert, J. C. and Lemaréchal, C.: Some numerical experiments with variable-storage quasi-Newton algorithms, Mathematical Programming, 45, 407–435, https://doi.org/10.1007/BF01589113, 1989.

GLOBALVIEW-CH4: Cooperative Atmospheric Data Integration Project – Methane, CD-ROM, also available on Internet via anonymous FTP to ftp.cmdl.noaa.gov, Path: ccg/ch4/GLOBALVIEW, NOAA ESRL, Boulder, Colorado, 2009.

Gurney, K. R., Law, R. M., Denning, A. S., Rayner, P. J., Baker, D., Bousquet, P., Bruhwiler, L., Chen, Y.-H., Ciais, P., Fan, S., Fung, I. Y., Gloor, M., Heimann, M., Higuchi, K., John, J., Maki, T., Maksyutov, S., Masarie, K., Peylin, P., Prather, M., Sarmiento, J., Taguchi, S., Takahashi, T., and Yuen, C.-W.: Towards robust regional estimates of CO_2 sources and sinks using atmospheric transport models, 415, 5, 2002.

Holmes, M. E., Sansone, F. J., Rust, T. M., and Popp, B. N.: Methane production, consumption, and air-sea exchange in the open ocean: An Evaluation based on carbon isotopic ratios, Global Biogeochemical Cycles, 14, 1–10, https://doi.org/10.1029/1999GB001209, 2000.

Hourdin, F., Musat, I., Bony, S., Braconnot, P., Codron, F., Dufresne, J.-L., Fairhead, L., Filiberti, M.-A., Friedlingstein, P., Grandpeix, J.-Y., Krinner, G., LeVan, P., Li, Z.-X., and Lott, F.: The LMDZ4 general circulation model: climate performance and sensitivity to parametrized physics with emphasis on tropical convection, Climate Dynamics, 27, 787–813, https://doi.org/10.1007/s00382-006-0158-0, 2006.

Houweling, S., Bergamaschi, P., Chevallier, F., Heimann, M., Kaminski, T., Krol, M., Michalak, A. M., and Patra, P.: Global inverse modeling of CH_4 sources and sinks: an overview of methods, Atmospheric Chemistry and Physics, 17, 235–256, https://doi.org/https://doi.org/10.5194/acp-17-235-2017, 2017.

Ide, K., Courtier, P., Ghil, M., and Lorenc, A. C.: Unified Notation for Data Assimilation : Operational, Sequential and Variational (gtSpecial IssueltData Assimilation in Meteology and Oceanography: Theory and Practice), Journal of the Meteorological Society of Japan. Ser. II, 75, 181–189, https://doi.org/10.2151/jmsj1965.75.1B_181, 1997.

Janssens-Maenhout, G., Crippa, M., Guizzardi, D., Muntean, M., Schaaf, E., Dentener, F., Bergamaschi, P., Pagliari, V., Olivier, J. G. J., Peters, J. A. H. W., Aardenne, J. A. v., Monni, S., Doering, U., and Petrescu, A. M. R.: EDGAR v4.3.2 Global Atlas of the three major Greenhouse Gas Emissions for the period 1970–2012, Earth System Science Data Discussions, pp. 1–55, https://doi.org/https://doi.org/10.5194/essd-2017-79, 2017.

Kirschke, S., Bousquet, P., Ciais, P., Saunois, M., Canadell, J. G., Dlugokencky, E. J., Bergamaschi, P., Bergmann, D., Blake, D. R., Bruhwiler, L., Cameron-Smith, P., Castaldi, S., Chevallier, F., Feng, L., Fraser, A., Heimann, M., Hodson, E. L., Houweling, S., Josse, B., Fraser, P. J., Krummel, P. B., Lamarque, J.-F., Langenfelds, R. L., Le Quéré, C., Naik, V., O'Doherty, S., Palmer, P. I., Pison, I., Plummer, D., Poulter, B., Prinn, R. G., Rigby, M., Ringeval, B., Santini, M., Schmidt, M., Shindell, D. T., Simpson, I. J., Spahni, R., Steele, L. P., Strode, S. A., Sudo, K., Szopa, S., van der Werf, G. R., Voulgarakis, A., van Weele, M., Weiss, R. F., Williams, J. E., and Zeng, G.: Three decades of global methane sources and sinks, Nature Geoscience, 6, 813–823, https://doi.org/10.1038/ngeo1955, 2013.

Klevenhusen, F., Bernasconi, S. M., Kreuzer, M., and Soliva, C. R.: Experimental validation of the Intergovernmental Panel on Climate Change default values for ruminant-derived methane and its carbon-isotope signature, Animal Production Science, 50, 159, https://doi.org/10.1071/AN09112, 2010.

Kort, E. A., Smith, M. L., Murray, L. T., Gvakharia, A., Brandt, A. R., Peischl, J., Ryerson, T. B., Sweeney, C., and Travis, K.: Fugitive emissions from the Bakken shale illustrate role of shale production in global ethane shift, Geophysical Research Letters, 43, 4617–4623, https://doi.org/https://doi.org/10.1002/2016GL068703, 2016.

Lambert, G. and Schmidt, S.: Reevaluation of the oceanic flux of methane: Uncertainties and long term variations, Chemosphere, 26, 579–589, https://doi.org/10.1016/0045-6535(93)90443-9, 1993.

Levin, I., Bergamaschi, P., Dörr, H., and Trapp, D.: Stable isotopic signature of methane from major sources in Germany, Chemosphere, 26, 161–177, https://doi.org/10.1016/0045-6535(93)90419-6, 1993.

Liu, X., Weinbren, A. L., Chang, H., Tadić, J., Mountain, M. E., Trudeau, M. E., Andrews, A. E., Chen, Z., and Miller, S. M.: Data reduction for inverse modeling: an adaptive approach v1.0, Geoscientific Model Development Discussions, pp. 1–21, https://doi.org/10.5194/gmd-2020-246, 2020.

Locatelli, R., Bousquet, P., Chevallier, F., Fortems-Cheney, A., Szopa, S., Saunois, M., Agusti-Panareda, A., Bergmann, D., Bian, H., Cameron-Smith, P., Chipperfield, M. P., Gloor, E., Houweling, S., Kawa, S. R., Krol, M., Patra, P. K., Prinn, R. G., Rigby, M., Saito, R., and Wilson, C.: Impact of transport model errors on the global and regional methane emissions estimated by inverse modelling, Atmospheric Chemistry and Physics, 13, 9917–9937, https://doi.org/https://doi.org/10.5194/acp-13-9917-2013, 2013.

Locatelli, R., Bousquet, P., Saunois, M., Chevallier, F., and Cressot, C.: Sensitivity of the recent methane budget to LMDz sub-grid-scale physical parameterizations, Atmospheric Chemistry and Physics, 15, 9765–9780, https://doi.org/10.5194/acp-15-9765-2015, 2015.

Louis, J.-F.: A parametric model of vertical eddy fluxes in the atmosphere, Boundary-Layer Meteorology, 17, 187–202, https://doi.org/10.1007/BF00117978, 1979.

Masarie, K. A. and Tans, P. P.: Extension and integration of atmospheric carbon dioxide data into a globally consistent measurement record, Journal of Geophysical Research: Atmospheres, 100, 11 593–11 610, https://doi.org/10.1029/95JD00859, 1995.

McNorton, J., Wilson, C., Gloor, M., Parker, R. J., Boesch, H., Feng, W., Hossaini, R., and Chipperfield, M. P.: Attribution of recent increases in atmospheric methane through 3-D inverse modelling, Atmospheric Chemistry and Physics, 18, 18 149–18 168, https://doi.org/https://doi.org/10.5194/acp-18-18149-2018, 2018.

Menut, L., Bessagnet, B., Khvorostyanov, D., Beekmann, M., Blond, N., Colette, A., Coll, I., Curci, G., Foret, G., Hodzic, A., Mailler, S., Meleux, F., Monge, J.-L., Pison, I., Siour, G., Turquety, S., Valari, M., Vautard, R., and Vivanco, M. G.: CHIMERE 2013: a model for regional atmospheric composition modelling, Geoscientific Model Development, 6, 981–1028, https://doi.org/10.5194/gmd-6-981-2013, 2013.

Neef, L., Weele, M. v., and Velthoven, P. v.: Optimal estimation of the present-day global methane budget, Global Biogeochemical Cycles, 24, https://doi.org/10.1029/2009GB003661, 2010.

Newsam, G. N. and Enting, I. G.: Inverse problems in atmospheric constituent studies. I. Determination of surface sources under a diffusive transport approximation, Inverse Problems, 4, 1037–1054, https://doi.org/10.1088/0266-5611/4/4/008, 1988.

Nisbet, E. G., Manning, M. R., Dlugokencky, E. J., Fisher, R. E., Lowry, D., Michel, S. E., Myhre, C. L., Platt, S. M., Allen, G., Bousquet, P., Brownlow, R., Cain, M., France, J. L., Hermansen, O., Hossaini, R., Jones, A. E., Levin, I., Manning, A. C., Myhre, G., Pyle, J. A., Vaughn, B. H., Warwick, N. J., and White, J. W. C.: Very Strong Atmospheric Methane Growth in the 4 Years 2014–2017: Implications for the Paris Agreement, Global Biogeochemical Cycles, 33, 318–342, https://doi.org/10.1029/2018GB006009, 2019.

Patra, P. K., Houweling, S., Krol, M., Bousquet, P., Belikov, D., Bergmann, D., Bian, H., Cameron-Smith, P., Chipperfield, M. P., Corbin, K., Fortems-Cheiney, A., Fraser, A., Gloor, E., Hess, P., Ito, A., Kawa, S. R., Law, R. M., Loh, Z., Maksyutov, S., Meng, L., Palmer, P. I., Prinn, R. G., Rigby, M., Saito, R., and Wilson, C.: TransCom model simulations of CH_4 and related species: linking transport, surface flux and chemical loss with CH_4 variability in the troposphere and lower stratosphere, Atmospheric Chemistry and Physics, 11, 12 813–12 837, https://doi.org/10.5194/acp-11-12813-2011, 2011.

Peters, W., Miller, J. B., Whitaker, J., Denning, A. S., Hirsch, A., Krol, M. C., Zupanski, D., Bruhwiler, L., and Tans, P. P.: An ensemble data assimilation system to estimate CO_2 surface fluxes from atmospheric trace gas observations, Journal of Geophysical Research: Atmospheres, 110, https://doi.org/https://doi.org/10.1029/2005JD006157, 2005.

Pison, I., Bousquet, P., Chevallier, F., Szopa, S., and Hauglustaine, D.: Multi-species inversion of CH_4, CO and H2 emissions from surface measurements, Atmos. Chem. Phys., p. 17, 2009.

Poulter, B., Bousquet, P., Canadell, J. G., Ciais, P., Peregon, A., Saunois, M., Arora, V. K., Beerling, D. J., Brovkin, V., Jones, C. D., Joos, F., Gedney, N., Ito, A., Kleinen, T., Koven, C. D., McDonald, K., Melton, J. R., Peng, C., Peng, S., Prigent, C., Schroeder, R., Riley, W. J., Saito, M., Spahni, R., Tian, H., Taylor, L., Viovy, N., Wilton, D., Wiltshire, A., Xu, X., Zhang, B., Zhang, Z., and Zhu, Q.: Global wetland contribution to 2000–2012 atmospheric methane growth rate dynamics, Environmental Research Letters, 12, 094 013, https://doi.org/10.1088/1748-9326/aa8391, 2017.

Rayner, P. J., Michalak, A. M., and Chevallier, F.: Fundamentals of data assimilation applied to biogeochemistry, Atmospheric Chemistry and Physics, 19, 13 911–13 932, https://doi.org/10.5194/acp-19-13911-2019, 2019.

Rice, A. L., Butenhoff, C. L., Teama, D. G., Röger, F. H., Khalil, M. A. K., and Rasmussen, R. A.: Atmospheric methane isotopic record favors fossil sources flat in 1980s and 1990s with recent increase, Proceedings of the National Academy of Sciences, 113, 10 791–10 796, https://doi.org/10.1073/pnas.1522923113, 2016.

Rigby, M., Manning, A. J., and Prinn, R. G.: The value of high-frequency, high-precision methane isotopologue measurements for source and sink estimation, Journal of Geophysical Research: Atmospheres, 117, https://doi.org/10.1029/2011JD017384, 2012.

Rigby, M., Montzka, S. A., Prinn, R. G., White, J. W. C., Young, D., O'Doherty, S., Lunt, M. F., Ganesan, A. L., Manning, A. J., Simmonds, P. G., Salameh, P. K., Harth, C. M., Mühle, J., Weiss, R. F., Fraser, P. J., Steele, L. P., Krummel, P. B., McCulloch, A., and Park, S.: Role of atmospheric oxidation in recent methane growth, Proceedings of the National Academy of Sciences, 114, 5373–5377, https://doi.org/10.1073/pnas.1616426114, 2017.

Rodenbeck, C., Houweling, S., Gloor, M., and Heimann, M.: CO_2 flux history 1982–2001 inferred from atmospheric data using a global inversion of atmospheric transport, Atmos. Chem. Phys., p. 46, 2003.

Sansone, F. J., Popp, B. N., Gasc, A., Graham, A. W., and Rust, T. M.: Highly elevated methane in the eastern tropical North Pacific and associated isotopically enriched fluxes to the atmosphere, Geophysical Research Letters, 28, 4567–4570, https://doi.org/10.1029/2001GL013460, 2001.

Saunois, M., Bousquet, P., Poulter, B., Peregon, A., Ciais, P., Canadell, J. G., Dlugokencky, E. J., Etiope, G., Bastviken, D., Houweling, S., Janssens-Maenhout, G., Tubiello, F. N., Castaldi, S., Jackson, R. B., Alexe, M., Arora, V. K., Beerling, D. J., Bergamaschi, P., Blake, D. R., Brailsford, G., Bruhwiler, L., Crevoisier, C., Crill, P., Covey, K., Frankenberg, C., Gedney, N., Höglund-Isaksson, L., Ishizawa, M., Ito, A., Joos, F., Kim, H.-S., Kleinen, T., Krummel, P., Lamarque, J.-F., Langenfelds, R., Locatelli, R., Machida, T., Maksyutov, S., Melton, J. R., Morino, I., Naik, V., O'Doherty, S., Parmentier, F.-J. W., Patra, P. K., Peng, C., Peng, S., Peters, G. P., Pison, I., Prinn, R., Ramonet, M., Riley, W. J., Saito, M., Santini, M., Schroeder, R., Simpson, I. J., Spahni, R., Takizawa, A., Thornton, B. F., Tian, H., Tohjima, Y., Viovy, N., Voulgarakis, A., Weiss, R., Wilton, D. J., Wiltshire, A., Worthy, D., Wunch, D., Xu, X., Yoshida, Y., Zhang, B., Zhang, Z., and Zhu, Q.: Variability and quasi-decadal changes in the methane budget over the period 2000–2012, Atmospheric Chemistry and Physics, 17, 11 135–11 161, https://doi.org/https://doi.org/10.5194/acp-17-11135-2017, 2017.

Saunois, M., Stavert, A. R., Poulter, B., Bousquet, P., Canadell, J. G., Jackson, R. B., Raymond, P. A., Dlugokencky, E. J., Houweling, S., Patra, P. K., Ciais, P., Arora, V. K., Bastviken, D., Bergamaschi, P., Blake, D. R., Brailsford, G., Bruhwiler, L., Carlson, K. M., Carrol, M., Castaldi, S., Chandra, N., Crevoisier, C., Crill, P. M., Covey, K., Curry, C. L., Etiope, G., Frankenberg, C., Gedney, N., Hegglin, M. I., Höglund-Isaksson, L., Hugelius, G., Ishizawa, M., Ito, A., Janssens-Maenhout, G., Jensen, K. M., Joos, F., Kleinen, T., Krummel, P. B., Langenfelds, R. L., Laruelle, G. G., Liu, L., Machida, T., Maksyutov, S., McDonald, K. C., McNorton, J., Miller, P. A., Melton, J. R., Morino, I., Müller, J., Murguia-Flores, F., Naik, V., Niwa, Y., Noce, S., O'Doherty, S., Parker, R. J., Peng, C., Peng, S., Peters, G. P., Prigent, C., Prinn, R., Ramonet, M., Regnier, P., Riley, W. J., Rosentreter, J. A., Segers, A., Simpson, I. J., Shi, H., Smith, S. J., Steele, L. P., Thornton, B. F., Tian, H., Tohjima, Y., Tubiello, F. N., Tsuruta, A., Viovy, N., Voulgarakis, A., Weber, T. S., van Weele, M., van der Werf, G. R., Weiss, R. F., Worthy, D., Wunch, D., Yin, Y., Yoshida, Y., Zhang, W., Zhang, Z., Zhao, Y., Zheng, B., Zhu, Q., Zhu, Q., and Zhuang, Q.: The Global Methane Budget 2000–2017, Earth System Science Data, 12, 1561–1623, https://doi.org/https://doi.org/10.5194/essd-12-1561-2020, 2020.

Schaefer, H., Fletcher, S. E. M., Veidt, C., Lassey, K. R., Brailsford, G. W., Bromley, T. M., Dlugokencky, E. J., Michel, S. E., Miller, J. B., Levin, I., Lowe, D. C., Martin, R. J., Vaughn, B. H., and White, J. W. C.: A 21st-century shift from fossil-fuel to biogenic methane emissions indicated by $^{13}CH_4$, Science, 352, 80–84, https://doi.org/10.1126/science.aad2705, 2016.

Schwietzke, S., Sherwood, O. A., Bruhwiler, L. M. P., Miller, J. B., Etiope, G., Dlugokencky, E. J., Michel, S. E., Arling, V. A., Vaughn, B. H., White, J. W. C., and Tans, P. P.: Upward revision of global fossil fuel methane emissions based on isotope database, Nature, 538, 88–91, https://doi.org/10.1038/nature19797, 2016.

Sherwood, O. A., Schwietzke, S., Arling, V. A., and Etiope, G.: Global Inventory of Gas Geochemistry Data from Fossil Fuel, Microbial and Burning Sources, version 2017, Earth System Science Data, 9, 639–656, https://doi.org/10.5194/essd-9-639-2017, 2017.

Smith, M. L., Kort, E. A., Karion, A., Sweeney, C., Herndon, S. C., and Yacovitch, T. I.: Airborne Ethane Observations in the Barnett Shale: Quantification of Ethane Flux and Attribution of Methane Emissions, Environmental Science & Technology, 49, 8158–8166, https://doi.org/10.1021/acs.est.5b00219, 2015.

Tans, P. P.: A note on isotopic ratios and the global atmospheric methane budget, Global Biogeochemical Cycles, 11, 77–81, https://doi.org/10.1029/96GB03940, 1997.

Thanwerdas, J., Saunois, M., Berchet, A., Pison, I., Hauglustaine, D., Ramonet, M., Crevoisier, C., Baier, B., Sweeney, C., and Bousquet, P.: Impact of atomic chlorine on the modelling of total methane and its $^{13}C:^{12}C$ isotopic ratio at global scale, Atmospheric Chemistry and Physics Discussions, 2019, 1–28, https://doi.org/10.5194/acp-2019-925, 2019.

Thompson, R. L., Nisbet, E. G., Pisso, I., Stohl, A., Blake, D., Dlugokencky, E. J., Helmig, D., and White, J. W. C.: Variability in Atmospheric Methane From Fossil Fuel and Microbial Sources Over the Last Three Decades, Geophysical Research Letters, 45, 11,499–11,508, https://doi.org/10.1029/2018GL078127, 2018.

Tiedtke, M.: A Comprehensive Mass Flux Scheme for Cumulus Parameterization in Large-Scale Models, Monthly Weather Review, 117, 1779–1800, https://doi.org/10.1175/1520-0493(1989)117<1779:ACMFSF>2.0.CO;2, 1989.

Townsend-Small, A., Tyler, S. C., Pataki, D. E., Xu, X., and Christensen, L. E.: Isotopic measurements of atmospheric methane in Los Angeles, California, USA: Influence of "fugitive" fossil fuel emissions, Journal of Geophysical Research: Atmospheres, 117, https://doi.org/10.1029/2011JD016826, 2012.

Turner, A. J., Frankenberg, C., Wennberg, P. O., and Jacob, D. J.: Ambiguity in the causes for decadal trends in atmospheric methane and hydroxyl, p. 6, 2017.

van der Werf, G. R., Randerson, J. T., Giglio, L., van Leeuwen, T. T., Chen, Y., Rogers, B. M., Mu, M., van Marle, M. J. E., Morton, D. C., Collatz, G. J., Yokelson, R. J., and Kasibhatla, P. S.: Global fire emissions estimates during 1997–2016, Earth System Science Data, 9, 697–720, https://doi.org/10.5194/essd-9-697-2017, 2017.

Warwick, N. J., Cain, M. L., Fisher, R., France, J. L., Lowry, D., Michel, S. E., Nisbet, E. G., Vaughn, B. H., White, J. W. C., and Pyle, J. A.: Using $\delta^{13}C$-CH_4 and δD-CH_4 to constrain Arctic methane emissions, Atmospheric Chemistry and Physics, 16, 14 891–14 908, https://doi.org/10.5194/acp-16-14891-2016, 2016.

Yver, C. E., Pison, I. C., Fortems-Cheiney, A., Schmidt, M., Chevallier, F., Ramonet, M., Jordan, A., Søvde, O. A., Engel, A., Fisher, R. E., Lowry, D., Nisbet, E. G., Levin, I., Hammer, S., Necki, J., Bartyzel, J., Reimann, S., Vollmer, M. K., Steinbacher, M., Aalto, T., Maione, M., Arduini, J., O'Doherty, S., Grant, A., Sturges, W. T., Forster, G. L., Lunder, C. R., Privalov, V., Paramonova, N., Werner, A., and Bousquet, P.: A new estimation of the recent tropospheric molecular hydrogen budget using atmospheric observations and variational inversion, Atmospheric Chemistry and Physics, 11, 3375–3392, https://doi.org/10.5194/acp-11-3375-2011, 2011.

Zazzeri, G., Lowry, D., Fisher, R. E., France, J. L., Lanoisellé, M., Kelly, B. F. J., Necki, J. M., Iverach, C. P., Ginty, E., Zimnoch, M., Jasek, A., and Nisbet, E. G.: Carbon isotopic signature of coal-derived methane emissions to the atmosphere:from coalification to alteration, Atmospheric Chemistry and Physics, 16, 13 669–13 680, https://doi.org/10.5194/acp-16-13669-2016, 2016.

Zupanski, D., Hou, A. Y., Zhang, S. Q., Zupanski, M., Kummerow, C. D., and Cheung, S. H.: Applications of information theory in ensemble data assimilation, Quarterly Journal of the Royal Meteorological Society, 133, 1533–1545, https://doi.org/https://doi.org/10.1002/qj.123, 2007.